Geochemistry Geophysics Geosystems G3
AN ELECTRONIC JOURNAL OF THE EARTH SCIENCES
Published by AGU and the Geochemical Society

Article
Volume 10, Number 10
10 October 2009
Q10001, doi:10.1029/2009GC002586
ISSN: 1525-2027

Click Here for Full Article

Heterogeneous seismic velocity structure of the upper lithosphere at Kane oceanic core complex, Mid-Atlantic Ridge

Min Xu
Massachusetts Institute of Technology–Woods Hole Oceanographic Institution Joint Program, Woods Hole, Massachusetts 02543, USA (minxu@mit.edu)

J. Pablo Canales, Brian E. Tucholke, and David L. DuBois
Department of Geology and Geophysics, Woods Hole Oceanographic Institution, Woods Hole, Massachusetts 02543, USA

[1] The Kane oceanic core complex (OCC) is a large, corrugated megamullion that was formed by a long-lived detachment fault at the axis of the Mid-Atlantic Ridge adjacent to Kane Fracture Zone between 2.1 and 3.3 Ma. We use refracted arrivals recorded along a 6-km-long hydrophone streamer during a multichannel seismic survey to constrain the shallow seismic velocity structure of the OCC. Results are presented in high-resolution traveltime seismic tomographic models along six lines that cover all of the main morphological features of the megamullion. The models show large lateral variability in *P* wave velocity within the upper ~0.5–2.0 km of the lithosphere, and these variations correlate to first order with observed variations in lithology, documented by in situ basement samples and seafloor morphology. Lithological interpretation of the velocity models indicates that there is marked lateral variability in distribution of gabbroic intrusions, serpentinized peridotites, and basalts at scales of a few kilometers to ~10 km. Serpentinized peridotites appear to dominate the central and older parts of the OCC. High-velocity gabbros are consistently (but not exclusively) present closer to the termination of the Kane detachment fault and toward the ends of the OCC. The structure of the lithosphere exhumed by the Kane detachment fault is far from the standard ophiolite-based Penrose model, and it does not show segment-centered magmatism that is commonly interpreted at slow spreading ridges. If the gabbros exhumed toward the termination of the OCC were emplaced deep (~10 km) beneath the spreading axis, they may have constituted a weak zone that focused initiation of the Kane detachment fault. Alternately, as the OCC footwall was being exhumed the gabbros may have been emplaced because of dynamic changes in melt supply, changes in mantle fertility, or decompression melting. Late stage volcanism is clearly associated with a major high-angle normal fault that cuts the detachment surface; this volcanism may have been stimulated or enhanced by bending stresses in the bending footwall. The shape of the large-scale corrugated morphology of the OCC is nearly invariant in the dip direction across major changes in basement lithology, indicating that once established, the form of the Kane detachment fault was highly resistant to modification.

Components: 15,812 words, 21 figures.

Keywords: Kane oceanic core complex; ocean crustal structure; detachment faulting; Mid-Atlantic Ridge; seismic tomography; lithology.

Index Terms: 3045 Marine Geology and Geophysics: Seafloor morphology, geology, and geophysics; 7270 Seismology: Tomography (6982, 8180); 7218 Seismology: Lithosphere (1236).

Received 27 April 2009; **Revised** 1 July 2009; **Accepted** 10 July 2009; **Published** 10 October 2009.

Copyright 2009 by the American Geophysical Union

Xu, M., J. P. Canales, B. E. Tucholke, and D. L. DuBois (2009), Heterogeneous seismic velocity structure of the upper lithosphere at Kane oceanic core complex, Mid-Atlantic Ridge, *Geochem. Geophys. Geosyst.*, *10*, Q10001, doi:10.1029/2009GC002586.

1. Introduction

[2] Footwalls of long-lived, or "detachment" faults at mid-ocean ridges (MORs) uplift and expose deep sections of the oceanic lithosphere on the seafloor [*Tucholke et al.*, 1996; *Cann et al.*, 1997; *Tucholke et al.*, 1998; *MacLeod et al.*, 2002] and form oceanic core complexes (OCCs). When the amount of the offset is sufficiently large, the footwalls roll over and form megamullions that are characterized by smooth dome-shaped surfaces and prominent spreading-parallel corrugations (mullion structures) that have amplitudes up to several hundred meters [*Tucholke et al.*, 1996, 1998]. Numerous OCCs in the form of megamullions have been identified along slow and intermediate spreading ridges [*Cann et al.*, 1997; *Tucholke et al.*, 1998; *Ohara et al.*, 2001; *Tucholke et al.*, 2001; *Reston et al.*, 2002; *Searle et al.*, 2003; *Okino et al.*, 2004; *Cannat et al.*, 2006; *Smith et al.*, 2006, 2008; *Tucholke et al.*, 2008], suggesting that exhumation of OCCs is a fundamental process in seafloor formation at MORs where melt supply is limited [*Smith et al.*, 2006; *Escartín et al.*, 2008; *Tucholke et al.*, 2008]. Most of these features are located at the ends of spreading segments where magmatism is inferred to be low [e.g., *Cannat et al.*, 1995a]. This observation led to the hypothesis that they form during periods of relatively amagmatic extension [e.g., *Tucholke et al.*, 1998]. However, drilling has shown that thick gabbro sections can be present in OCCs [*Dick et al.*, 2000; *Kelemen et al.*, 2004; *Blackman et al.*, 2006], and it recently has been proposed that OCCs form when moderate amounts of total plate separation are accommodated by magmatism [*Buck et al.*, 2005; *Tucholke et al.*, 2008].

[3] Both gabbros and peridotites are abundant at OCCs [e.g., *Tucholke et al.*, 1998], which suggests that OCCs may be excellent locations to study melt generation and migration in the mantle, as well as crustal accretion processes [e.g., *Dick et al.*, 2008]. However, there generally are poor constraints on how lithologies are distributed across and especially beneath OCCs. Seafloor sampling of OCCs is usually restricted to the exposed detachment surface where abundant allochthonous rocks of unknown provenance are present; only in areas where the detachment is cut by high-angle normal faults or slide scar headwalls is the underlying bedrock exposed. Deep drilling has been accomplished at three OCCs [*Dick et al.*, 2000; *Kelemen et al.*, 2004; *Blackman et al.*, 2006] and has recovered dominantly gabbroic sequences up to 1.4 km thick that may or may not be representative of the OCCs as a whole.

[4] To better understand lithological relations within OCCs, it is useful to employ remote geophysical methods to obtain broad coverage, to map lateral and vertical variations in rock properties, and to correlate these variations to changes in lithology as documented by in situ samples. In this paper we present results from a detailed seismic study of the OCC at Kane megamullion, which is one of the best developed and most sampled OCCs on the Mid-Atlantic Ridge (MAR) (Figure 1). Our work builds upon and expands that of *Canales et al.* [2008], who presented a comparative seismic study of three MAR OCCs (including the Kane OCC). Seismic tomography models along six strike and dip profiles over the Kane OCC show large lateral variations in velocity structure within the upper 1–2 km of lithosphere. There is an excellent correlation between seismic structure and lithology of in situ basement samples, which allows us to infer the large-scale distribution of the dominant lithologies across the Kane OCC. We use the seismically inferred spatial distribution of gabbroic intrusions, serpentinized peridotites, and volcanic rocks to provide new insights into the origin and evolution of the Kane OCC, as well as into the general process of magmatic accretion within segments of slow spreading ridges.

2. Background

2.1. Previous Seismic Tomographic Studies of MAR OCCs

[5] *Canales et al.* [2008] presented seismic tomography models derived from large-offset (6 km) multichannel seismic (MCS) data for three of the best developed OCCs known along the MAR: Atlantis Massif, Dante's Domes, and Kane OCC. Using only two profiles (orthogonal to each other

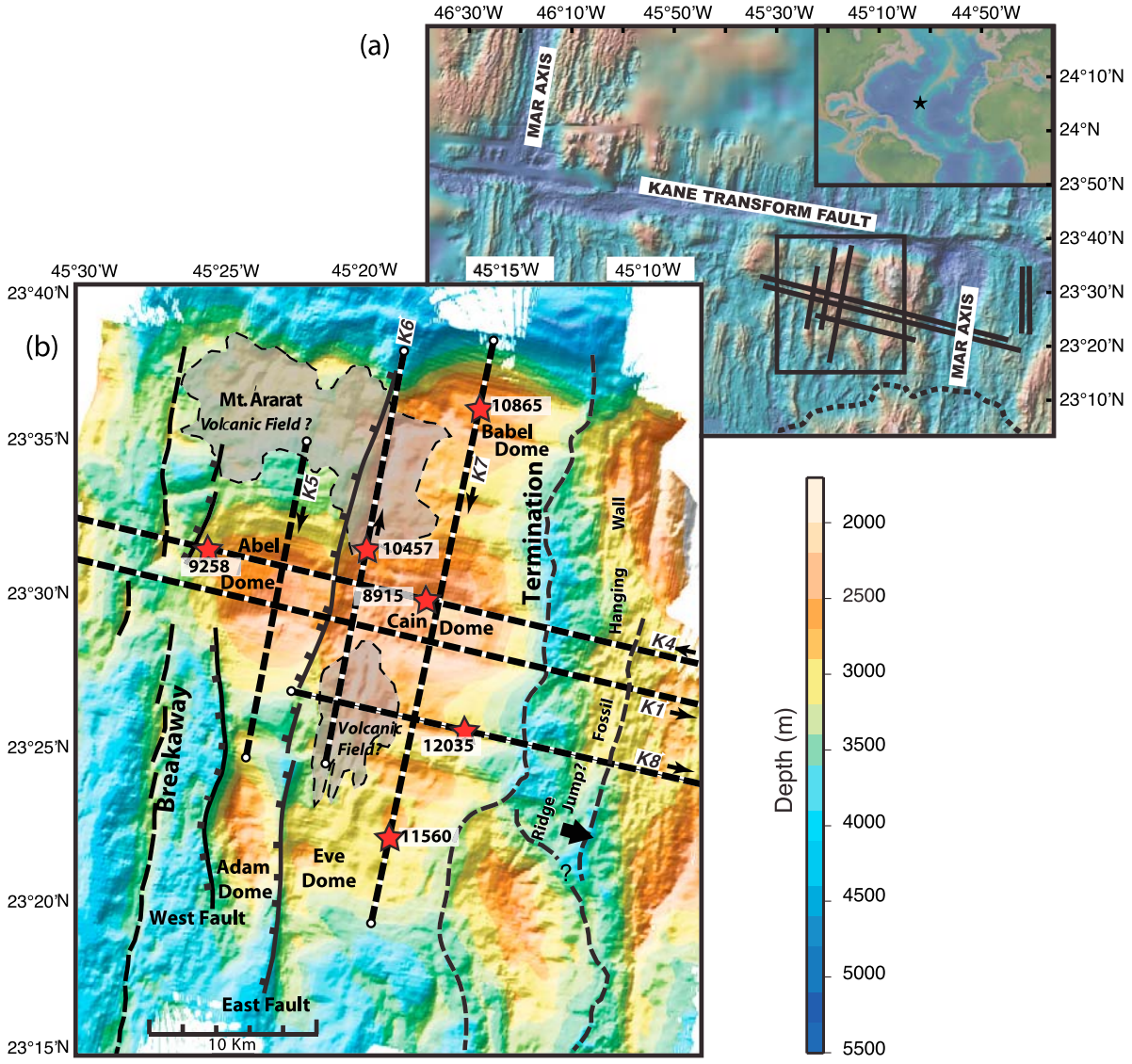

Figure 1. (a) Shaded relief bathymetry of the Mid-Atlantic Ridge (MAR) around Kane Transform Fault. Data are from the Marine Geoscience Data System (http://www.marine-geo.org/). The star in the inset shows the study location on the MAR. The Kane OCC study area (expanded view in Figure 1b) is outlined by a box, and black lines show eight multichannel seismic lines that were acquired during cruise EW0102. A nontransform discontinuity marking the southern boundary of the spreading segment that contains the Kane OCC is shown by a dotted line. (b) Bathymetric map and simplified tectonic interpretation of the Kane OCC based on SeaBeam bathymetry from R/V *Knorr* Cruise 180-2 (adapted from *Dick et al.* [2008]). Straight dashed lines locate seismic profiles with shooting direction indicated by arrows. Red stars with shot numbers show positions of six shot gathers displayed in Figure 2. Other dashed lines show locations of the breakaway and termination of the Kane detachment fault. The whole detachment surface is cut by a west facing normal fault (East Fault), and other normal faults are indicated by ticked lines. Shaded regions outlined by dashes indicate areas of possible volcanic fields, interpreted on the basis of seafloor samples, morphology, and, where available, subseafloor velocity structure.

along the dip and strike directions) at each of the three OCCs, they reported the large-scale structural characteristics that are common to all of the studied OCCs, and therefore could be interpreted in terms of the general processes controlling the formation and evolution of OCCs. Their interpretations were based on the observation that the shallow (~0.5–1.7 km) *P* wave velocity structure of the OCCs could be broadly grouped into three classes, and that each class correlates with different footwall lithologies documented by in situ geological samples and seafloor morphology: class V1, corresponding to areas with low uppermost velocities (<3.4 km s^{-1}) and low vertical velocity gradients (<~1 s^{-1}),

correlates with volcanics and hummocky morphology; class V2, for areas with intermediate velocities (~3.4–4.2 km s^{-1}) and intermediate velocity gradients (1–3 s^{-1}), correlates with massive outcrops of dominantly serpentinized peridotite; and class V3, for areas with high velocities (>4.2 km s^{-1}) and large velocity gradients (>3 s^{-1}), corresponding to gabbros.

[6] This classification allowed *Canales et al.* [2008] to show that at MAR OCC gabbros are heterogeneously distributed as large (tens to >100 km^2) bodies within serpentinized peridotites, and that they are consistently present near the terminations of the detachment faults. They hypothesized that this fact could indicate enhanced magmatism during the late stages of OCC formation due either to natural variability in the magmatic cycle or decompression melting stimulated during rapid exhumation of the footwall.

2.2. Geological Setting of the Kane OCC

[7] The near-axis section of the MAR between the Kane Fracture Zone at 23°40′N and ~22°30′N (i.e., the MARK area) has been studied by numerous geophysical and geological investigations. These include SeaBeam bathymetric mapping of the Kane transform [*Pockalny et al.*, 1988] and the adjacent ridge axis extending south to ~22°30′N [*Kong et al.*, 1988], a Sea MARC I side-scan sonar survey of the inner rift valley [*Kong et al.*, 1988], submersible investigations and sampling of the northern rift valley and eastern Kane ridge-transform intersection [e.g., *Karson and Dick*, 1983; *Karson et al.*, 1987; *Brown and Karson*, 1988; *Mével et al.*, 1991; *Auzende et al.*, 1994], drilling (ODP Legs 109 [*Detrick et al.*, 1988] and 153 [*Cannat et al.*, 1995b]), and seismic refraction experiments in the Kane fracture zone [*Detrick and Purdy*, 1980; *Cormier et al.*, 1984] and in the rift valley to the south [*Purdy and Detrick*, 1986; *Canales et al.*, 2000a]. Magnetic anomaly profiles across the rift valley indicate asymmetric spreading during the last 3–4 Myr [*Schulz et al.*, 1988], with faster rates to the west (~14.1 mm/a) than to the east (~11.3 mm/a). This asymmetry has been caused by a series of small eastward ridge jumps [*Schulz et al.*, 1988]. Off-axis geophysical studies within and immediately to the south of the MARK area [*Gente et al.*, 1995; *Pockalny et al.*, 1995; *Maia and Gente*, 1998] have shown complex tectonic patterns generated by along-axis growth and contraction of spreading segments during the last 10 Myr.

[8] Bathymetric [*Kong et al.*, 1988], magnetic [*Schulz et al.*, 1988] and submersible data [*Karson et al.*, 1987; *Brown and Karson*, 1988] indicate that the MARK area consists of at least two distinct second-order segments that are separated by a nontransform discontinuity near ~23°10′N at the MAR axis [*Karson et al.*, 1987; *Kong et al.*, 1988; *Cannat et al.*, 1995a]. The northern segment is ~40 km long and highly asymmetrical at its northern end, with a prominent elevated inside-corner massif at the intersection of the rift valley with the Kane transform [*Karson and Dick*, 1983] (Figure 1). The western rift valley wall has large fault scarps that expose gabbros and serpentinized peridotites along most of the segment [e.g., *Mével et al.*, 1991]. This has been interpreted to represent the initial stages of formation of an OCC. The eastern flank is characterized by smaller faults and a continuous basaltic carapace that indicates volcanic constructional morphology [*Karson and Dick*, 1983; *Karson et al.*, 1987; *Kong et al.*, 1988]. Seismic reflection profiles over the rift valley of the northern segment have not provided conclusive evidence for melt accumulations within the axial crust [*Detrick et al.*, 1990; *Calvert*, 1995], but a seismic refraction profile suggests that the segment is presently magmatically active [*Canales et al.*, 2000a]. Mantle Bouguer anomalies in the MARK area [*Morris and Detrick*, 1991; *Ballu et al.*, 1998; *Maia and Gente*, 1998] are irregular and more complex than the simple "bull's eye" pattern that characterizes other parts of the MAR [*Lin et al.*, 1990; *Detrick et al.*, 1995].

[9] The Kane OCC is a large megamullion (~23 km by ~40 km in dip and strike directions, respectively) formed by a long-lived detachment fault between ~3.3 and 2.1 Ma [*Williams et al.*, 2006] (Figure 1). It is located immediately south of the Kane Transform Fault (TF), ~30–55 km off-axis on the western side of the northern MARK segment, occupying about two thirds of the length of the paleospreading segment (Figure 1). It shows the key features that characterize megamullions [*Tucholke et al.*, 1998]. The breakaway zone, where the detachment fault initially nucleated, correlates with a linear, isochron-parallel ridge that is continuous for more than 40 km (with the exception of a small offset near latitude 23° 30′N) (Figure 1). The exposed detachment fault constitutes the megamullion surface, which is dome-shaped and exhibits slip-parallel corrugations (mullion structures) up to a few hundred meters in amplitude. The termination is defined by a valley located between the smooth

detachment fault surface and the rough, younger terrain of the fossil hanging wall. The Kane OCC contains several domes (Babel, Abel, Cain, Adam, and Eve, following the nomenclature of *Dick et al.* [2008] (Figure 1)) that are elevated up to a kilometer or more above adjacent seafloor. The largest domes forming the central part of the OCC (Abel and Cain Domes) are separated by a major west dipping, high-angle normal fault that cuts the detachment surface (East Fault, Figure 1). Most of the geological sampling on the Kane OCC has been done by dredge and ROV on R/V *Knorr* cruise 180-2 [*Dick et al.*, 2008]; this is complemented by sampling done along the southern wall of the Kane TF (northern wall of the OCC) during submersible dives of the KANAUT Expedition [*Auzende et al.*, 1994]. Details of the lithological structure of the Kane OCC are given by *Dick et al.* [2008]. The extensive geological sampling of the Kane OCC provides an excellent opportunity to calibrate our seismic results according to lithology, and thus to interpret the broader scope of geological structure within the Kane OCC.

3. Data and Methods

3.1. Seismic Data Acquisition and Processing

[10] The MCS data used in this study were acquired in 2001 aboard R/V *Maurice Ewing* (cruise EW0102). Details of the data acquisition are in Appendix A. A total of eight MCS lines were acquired over the Kane OCC, across the MAR axis, and over conjugate crust east of the axis (Figure 1). We applied traveltime tomography methods to the streamer refracted arrivals in the recorded data to derive the subseafloor structure along the profiles [e.g., *Zelt et al.*, 2004]. We here present results from the six ~20- to 50-km-long profiles located over the Kane OCC. Data from profiles that cross the spreading axis and conjugate crust could not be used for our traveltime tomography analysis because the seafloor is too deep to observe subseafloor refractions in advance of seafloor reflections. Results from profiles K1 and K7 were recently published in a comparative study of several OCCs [*Canales et al.*, 2008]; here we expand the analysis to the remaining profiles. The MCS lines employed in this study include 3 dip lines (K4, K1, K8) and 3 strike lines (K5, K6, K7) (Figure 1). These six lines cover most of the main domes of the Kane OCC. The dip lines extend to the east across the hanging wall remnant, and two of them (K1 and K4) extend westward across the breakaway zone.

[11] The long shot-receiver offsets provided by the hydrophone steamer, combined with the relatively shallow seafloor depths across the Kane OCC, allowed us to record clear subseafloor refractions (Figure 2) that we use in traveltime tomography modeling. During data processing, we first edited out bad traces. In order to increase the signal-to-noise ratio (SNR), every five consecutive shots were gathered, and the common offset traces were stacked and averaged to form 480-fold "supershot gathers." The supershot gathers were filtered in the frequency–wave number domain to remove low-frequency cable noise, and they were band-pass filtered (minimum phase) with frequency bands of 3-5-15-30 Hz or 3-5-30-50 Hz, depending on the data quality. Figure 2 shows six representative supershot gathers located over areas with different seafloor geology. In general, shot gathers exhibit clear subseafloor refractions that arrive before the seafloor reflections at ranges larger than ~2–3 km. Note that as the water depth beneath the shot and streamer increases, the crossover distance between the seafloor reflection and subseafloor refracted first arrivals increases (e.g., profile K4 shot 9258 and shot 8915, Figure 2). Data quality is generally very good, although some areas exhibit poor SNR (e.g., profile K8 shot 12035, Figure 2). In such cases rough seafloor topography and complex subsurface structure may be affecting the propagation of seismic energy and thus reducing the SNR.

3.2. Traveltime Picks

[12] The data used in the tomographic modeling are *P* wave first-arrival traveltime picks. In some regions, it is possible to discern a number of secondary refracted branches from different layers (e.g., profile K6 shot 10457 and profile K7 shot 11560, Figure 2). However, in this study we focus our analysis on modeling the travel times of the first-arriving refractions that precede the direct water wave. Because we employ a 2-D analysis procedure, we use only data from shot-receiver pairs that are located approximately along the linear parts of the profiles, excluding shot-receiver pairs collected during ship turns and where feathering was excessive. All traveltime picks were made using a semiautomatic first-break picking method using the software Focus (Paradigm™). First, traveltimes were picked within a supershot gather and then extrapolated to the next 10 gathers, automatically adjusting to the nearest waveform

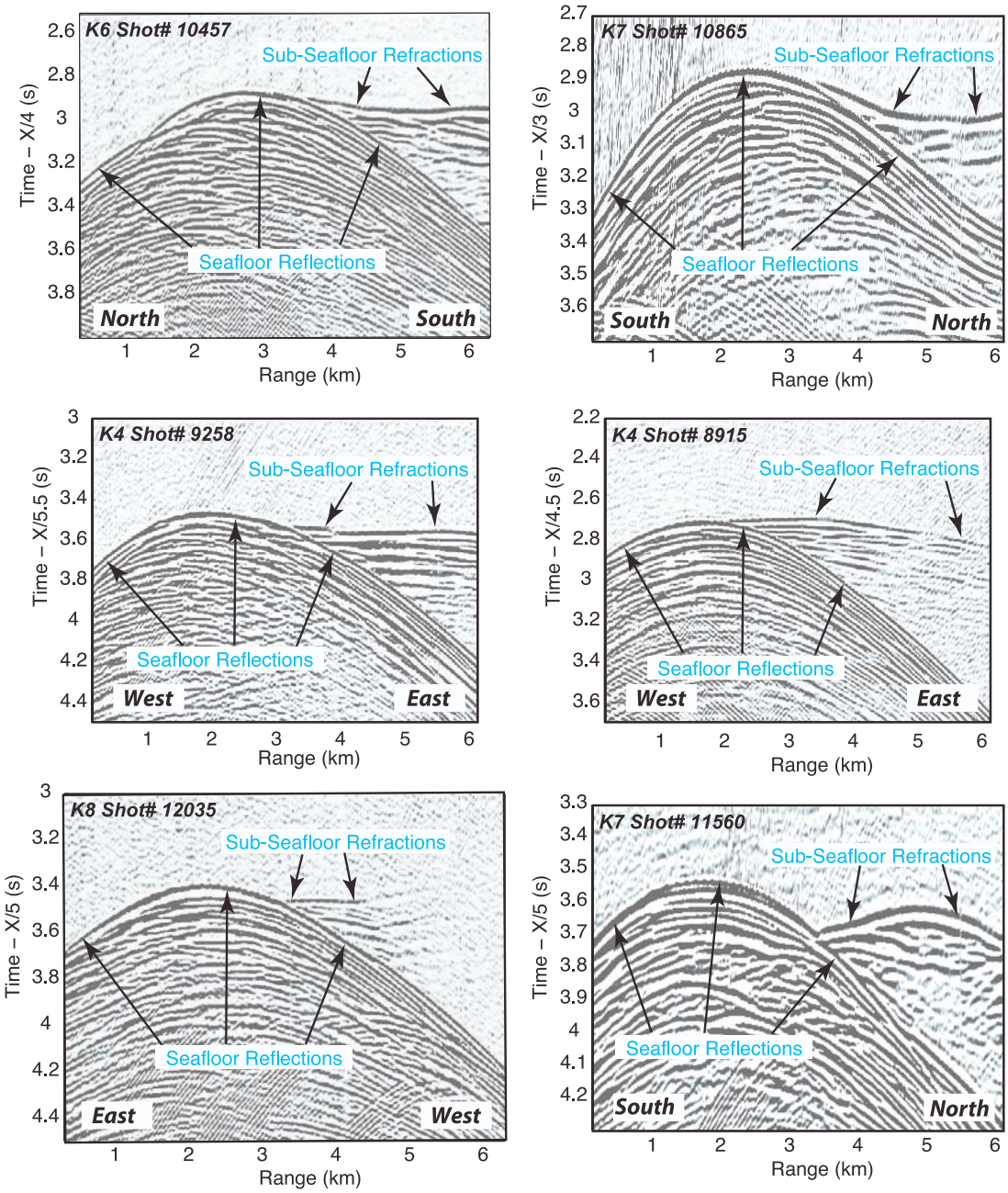

Figure 2. Six representative shot gathers from seismic profiles over the Kane OCC. Horizontal axes are distances from source to receivers along the streamer, and vertical axes are reduced two-way traveltime with different reduction velocities as indicated. Shot gather positions are shown in Figure 1 by red stars. In general, shot gathers of our data exhibit clear seafloor reflections and subseafloor refractions.

peak. Picks were then visually inspected and, if necessary, adjusted by hand. The accuracy of traveltime picking in noisy traces was improved by comparing the seismic signature with that of traces at similar offsets in nearby shots with higher SNR. This process guarantees consistency across all shots.

[13] Pick uncertainties were calculated on the basis of the SNR in a 100-ms window around the pick [*Zelt and Forsyth*, 1994]. As in the method of *Zelt and Forsyth* [1994], SNR was calculated as the square root of the ratio between the maximum trace amplitude in a 100-ms window before and after the pick. The relation between the SNR and the assigned traveltime uncertainty was established using the empirical equation $\sigma = 45 \cdot \mathrm{SNR}^{-0.9535}$, where σ represents traveltime uncertainty in milli-

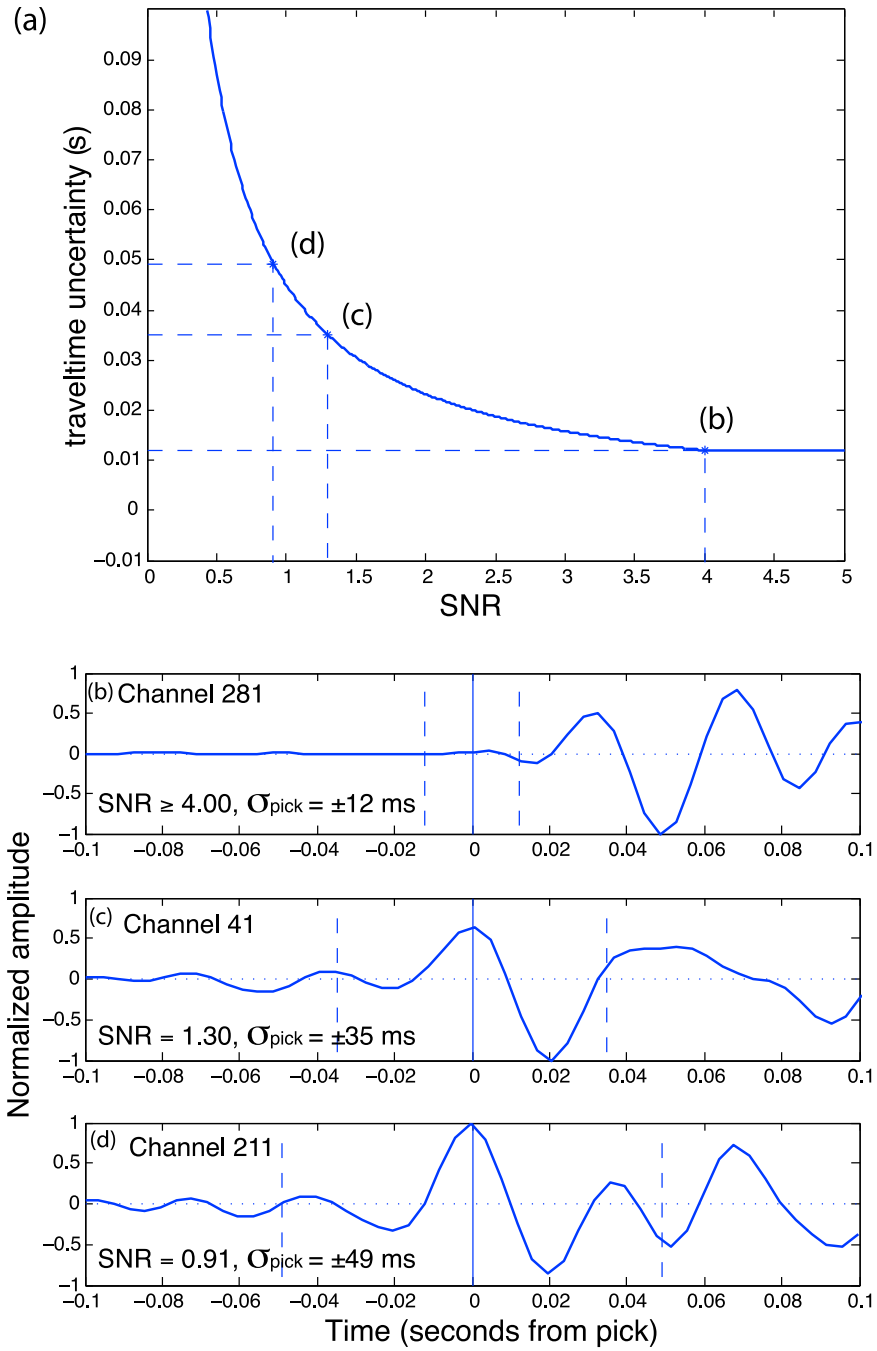

Figure 3. (a) Empirical relationship between signal-to-noise ratio (SNR) and traveltime uncertainty (σ). The three points on the curve represent three examples shown in Figures 3b–3d. For any traces with SNR $\geq$ 4.00, traveltime uncertainties were assigned as 12 ms. (b–d) Selected seismic traces from shot 11200 of profile K7, representing three different SNR values. Horizontal axis is time, with 0 s corresponding to the pick identification (vertical solid line). Vertical dashed lines indicate total traveltime uncertainties. Vertical axis is trace amplitude, normalized to the maximum value observed in the window displayed. Note that in Figure 3b seismic amplitudes are dominated by secondary high-amplitude seafloor reflections, making the pick amplitude appear small; however, amplitude of the traveltime pick is still significantly larger than that of the noise preceding the pick.

seconds (Figure 3a). Errors both in the shot-receiver offset and in seafloor depth at the ray entry point affect traveltime uncertainties, and we therefore adopted 12 ms (3 data samples) as the minimum traveltime uncertainty (uncertainties smaller than the minimum value were reassigned to 12 ms). In Figures 3b–3d we show three selected traces from shot 11200 of profile K7, together with their trav-

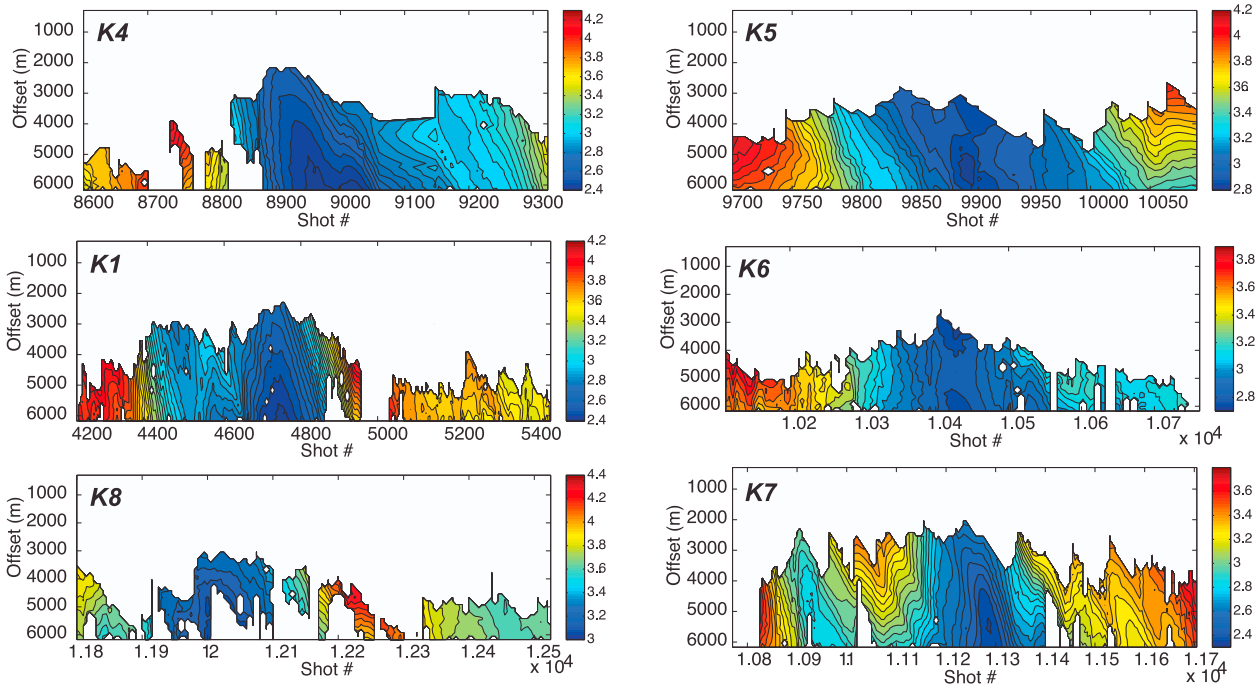

Figure 4. Picked first-arrival traveltimes (two-way traveltimes reduced at 3.7 km s^{-1}). A vertical column indicates the time along the streamer for a single shot. Near offsets (high channel numbers) are at the tops of the plots. In white regions, no traveltimes were picked for a particular shot-receiver pair because of noisy data or because subseafloor refractions arrive later than the seafloor reflection at short offsets. Contour interval is 0.1 s.

eltime picks and uncertainties representative of three different SNR values.

[14] Traveltime picks were decimated in the shot and receiver domains before the inversion to alleviate the computational load and because the original shot and receiver spacing is below the resolving power of ray theory (the radius of the first Fresnel zone at the seafloor is ~275 m, assuming an average seafloor depth of 3 km, a dominant frequency of 30 Hz and a velocity of 1.5 km/s). Therefore we used traveltime picks from one out of every 5 shot gathers, and from one out of every 10 receivers within each shot gather. The decimated sets of traveltime picks are shown in Figure 4 as color plots of traveltime versus shot number and source-receiver offset. Blue areas correspond to small traveltimes, which can be caused by either shallow water depth or high subseafloor velocity. The corresponding calculated traveltime uncertainties are shown in Figure 5. The plots of the pick uncertainties show that low uncertainty generally corresponds to smaller offsets.

3.3. Streamer Traveltime Tomography

[15] We performed 2-D tomographic inversions using first-arrival traveltimes recorded along the streamer [e.g., *Calvert et al.*, 2003; *Zelt et al.*, 2004]. Our objective was to derive the smoothest 2-D velocity model for each line, i.e., a model with the least amount of structure that fits the observed traveltimes within their uncertainty in the least number of iterations. We used the software FAST [*Zelt and Barton*, 1998] to obtain *P* wave velocity models by minimizing the data residuals and the roughness of perturbations from a background model. As a measure of the goodness of traveltime fit we use the weighted misfit function χ^2 defined as:

$$\chi^2 = \frac{1}{N}\sum_{i=1}^{N}\left(\frac{T_i^{obs} - T_i^{pre}}{T_i^{unc}}\right)^2,$$

where N is the total number of data, T_i^{obs} is the ith observed traveltime, T_i^{pre} is the ith predicted traveltime, and T_i^{unc} is traveltime uncertainty for the ith data point. Ideally $\chi^2 = 1$ indicates fitting of the observations within their uncertainties. The forward problem, ray tracing and traveltime calculation, was solved in a regular grid with 25 m node spacing both vertically and horizontally. Because of the water depth in the study area, the observed subseafloor refractions are not true first arrivals (first arrivals are actually direct waves

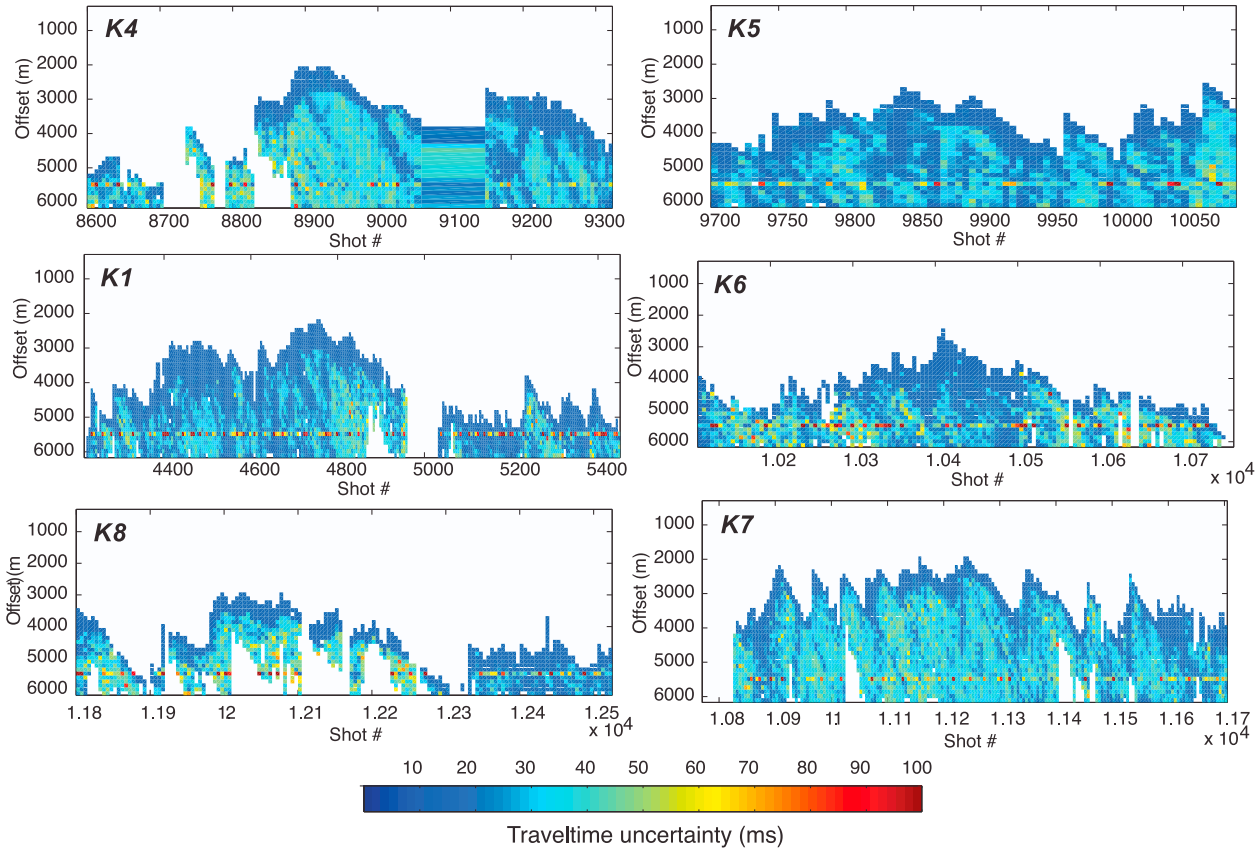

Figure 5. Pick uncertainties for traveltimes shown in Figure 4. The plot reveals regions of relatively low uncertainty as well as more diffuse regions of higher uncertainty. The higher uncertainty at 5500 m offset is due to a noisy channel on the streamer.

propagating from sources to receivers). Thus we use a modified ray-tracing algorithm in order to calculate raypaths and traveltimes only from subseafloor arrivals [*Canales et al.*, 2008].

[16] All the nonlinear inversions were performed on a uniform 200-m grid, using a regularized, damped least squares solution [*Zelt and Barton*, 1998]. The regularization is obtained by minimizing an objective function Φ(m):

$$\Phi(m) = \delta t^T C_d^{-1} \delta t + \lambda \left[m^T C_h^{-1} m + s_z m^T C_v^{-1} m \right]$$

where $\delta t^T C_d^{-1} \delta t$ are traveltime residuals (weighted by their uncertainty C_d); C_h and C_v are the horizontal and vertical second spatial partial derivatives, respectively, of the model parameters m. The tradeoff between minimizing traveltime residuals and obtaining a smooth solution is controlled by the damping parameter λ, and s_z controls the importance (weighting) of vertical versus horizontal smoothness [*Zelt and Barton*, 1998], with $s_z = 0$ indicating no smoothing in the vertical direction, $s_z = 1$ meaning equally vertical and horizontal smoothing, and $s_z > 1$ resulting in models with stronger vertical smoothing constraints.

[17] As a starting model, we use a simple model defined by a seafloor velocity and a constant vertical velocity gradient that represents the average 1-D structure of all our profiles (see Appendix B and Figure B1). The traveltime residuals predicted by the 1-D starting model are shown in Figure 6. The large positive (blue) and negative (red) residuals indicate that the 1-D model is a poor representation of the subseafloor structure; thus our data require large lateral velocity variations. On the basis of the traveltime residuals, we can anticipate that the dip profiles K1, K4, and K8 will be characterized by alternating regions with structures both faster and slower than the starting model, while the strike profiles will be characterized, on average, by a somewhat more homogeneous structure that is either faster (profile K7) or slower (profiles K5 and K6) than the starting model.

[18] Our preferred 2-D models (Figure 7) were chosen with different values of the damping parameter λ and iteration number for each profile

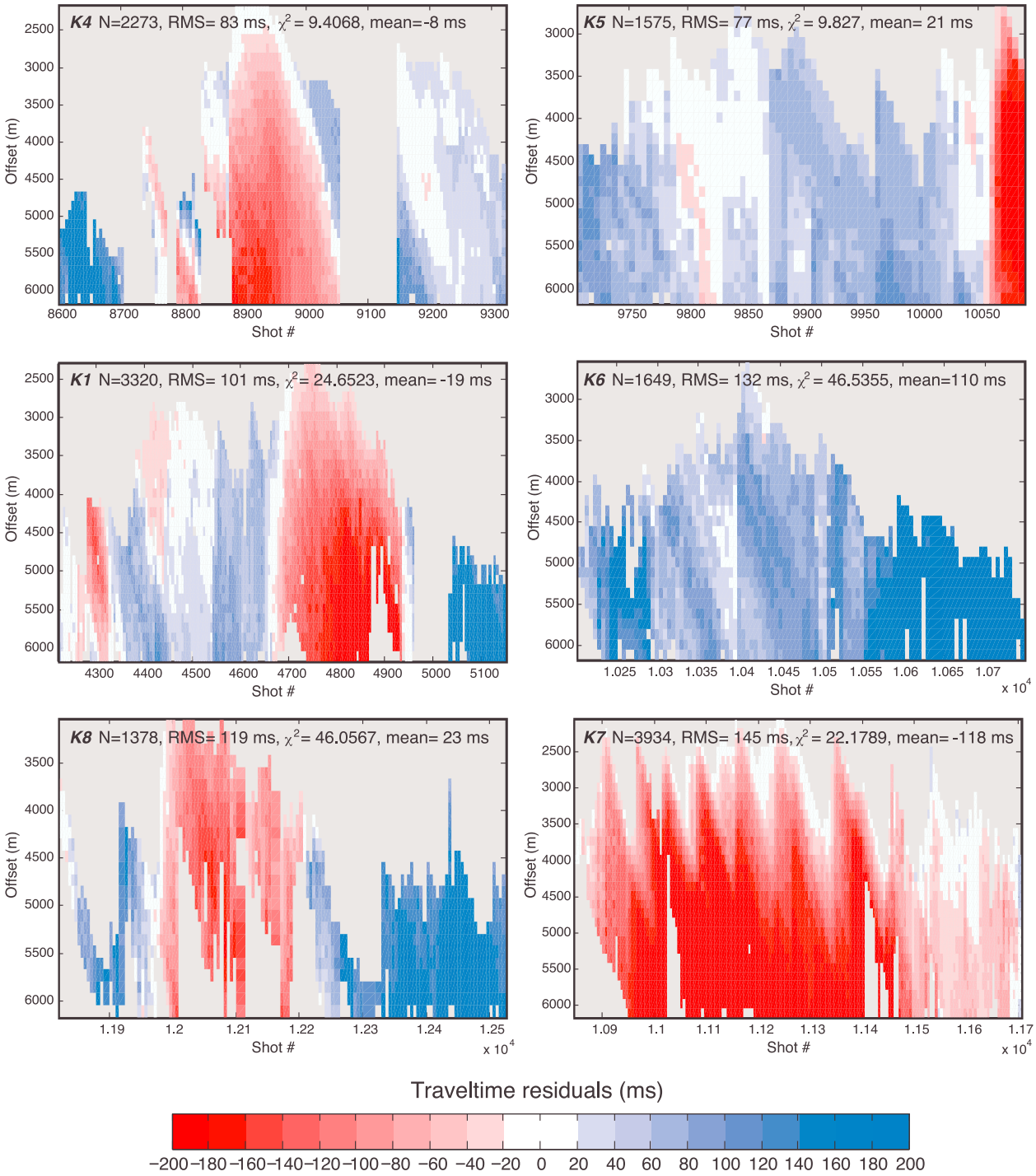

Figure 6. Color maps of traveltime residuals predicted from the initial 1-D starting model displayed as a function of shot number and source-receiver offset for each seismic profile. Color breaks are every 20 ms. Light gray indicates sections with no traveltime pick. N is number of observations, RMS is root-mean-squared traveltime residuals, χ^2 is weighted misfit function, and mean is the mean of the distributions.

(see Appendix B). This allows us to image seismic heterogeneities at different scales along each profile as the data may require different amounts of structure in each profile. We note that our preferred solution for profile K7 is somewhat different than that published by *Canales et al.* [2008], who used a smaller value of λ. However, the differences between these two acceptable models are minimal and do not affect the interpretation of this study or the study of *Canales et al.* [2008].

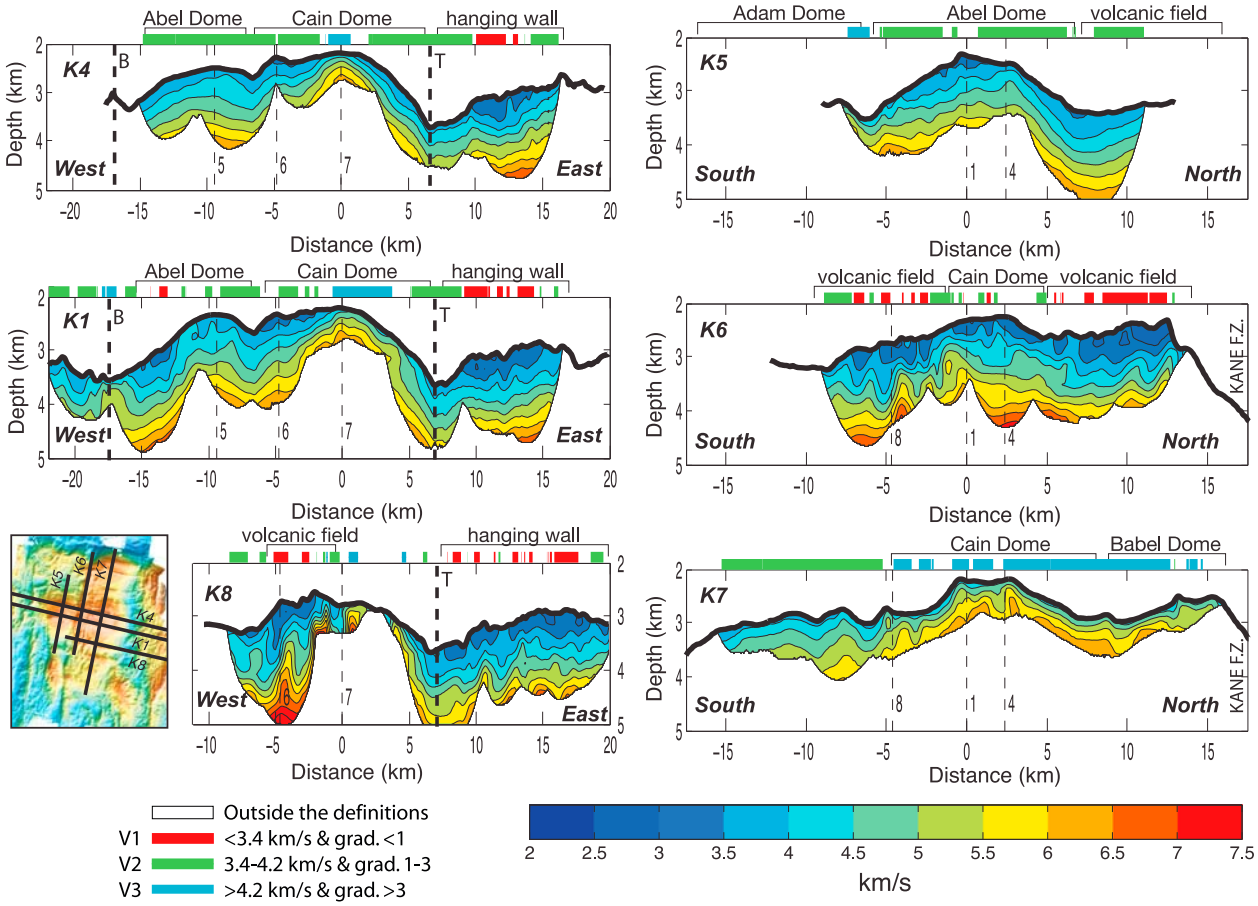

Figure 7. Two-dimensional tomographic models of *P* wave velocity beneath Kane OCC (profile locations are in the bottom left inset). Contour interval is 0.5 km s^{-1}. (left) Dip profiles and (right) strike profiles. Thicker dashed lines on dip profiles indicate locations of breakaway (B) and termination (T). Thinner dashed lines show crossings between dip and strike profiles. Dip profiles are aligned on the crossings of strike profile K7, and strike profiles are aligned on the crossings of dip profile K1. Morphological features are labeled at the top of the profiles. The along-profile extents of V1, V2, and V3 velocity characteristics in the upper ~500 m of the tomographic models are indicated by color bars at the top of each profile (key at bottom left; see section 4 for explanation). These three classes of velocity characteristics encompass most of the observed velocity structure.

[19] The preferred velocity models (Figure 7) are discussed in detail in section 4. Figure 8 shows the traveltime residuals calculated by subtracting traveltimes predicted from the preferred velocity models from the observed traveltimes. Note that, compared to Figure 6, the large positive and negative traveltime residuals predicted by the initial model have been largely reduced by the preferred models. The traveltime residuals are nearly evenly distributed, indicating that all the data are equally well fitted across all source-receiver offsets and shots, except at some locations with rougher topography and/or deeper seafloor (e.g., near shot 4900 along profile K1, Figure 8).

[20] The strong lateral variations in seismic velocity shown in the preferred models are required to fit the observed data and are not just simply consistent with the data. For example, Figure 9 shows an example of two representative shots for profile K4 that sample different velocity structures. Figure 9 (top) shows the observed supershot gathers with the observed traveltime picks and the predicted traveltime curves calculated from the initial and final models. The initial velocity model fits reasonably well the observed traveltimes for shot 9258, but it is too slow for shot 8915, indicating the presence of higher velocities beneath shot 8915. The final velocity model recovers such high velocity well and provides a good fit to the observed traveltimes. Figure 9 also shows the complete ray coverage for profile K4. Ray coverage is dense and relatively homogenous, except in

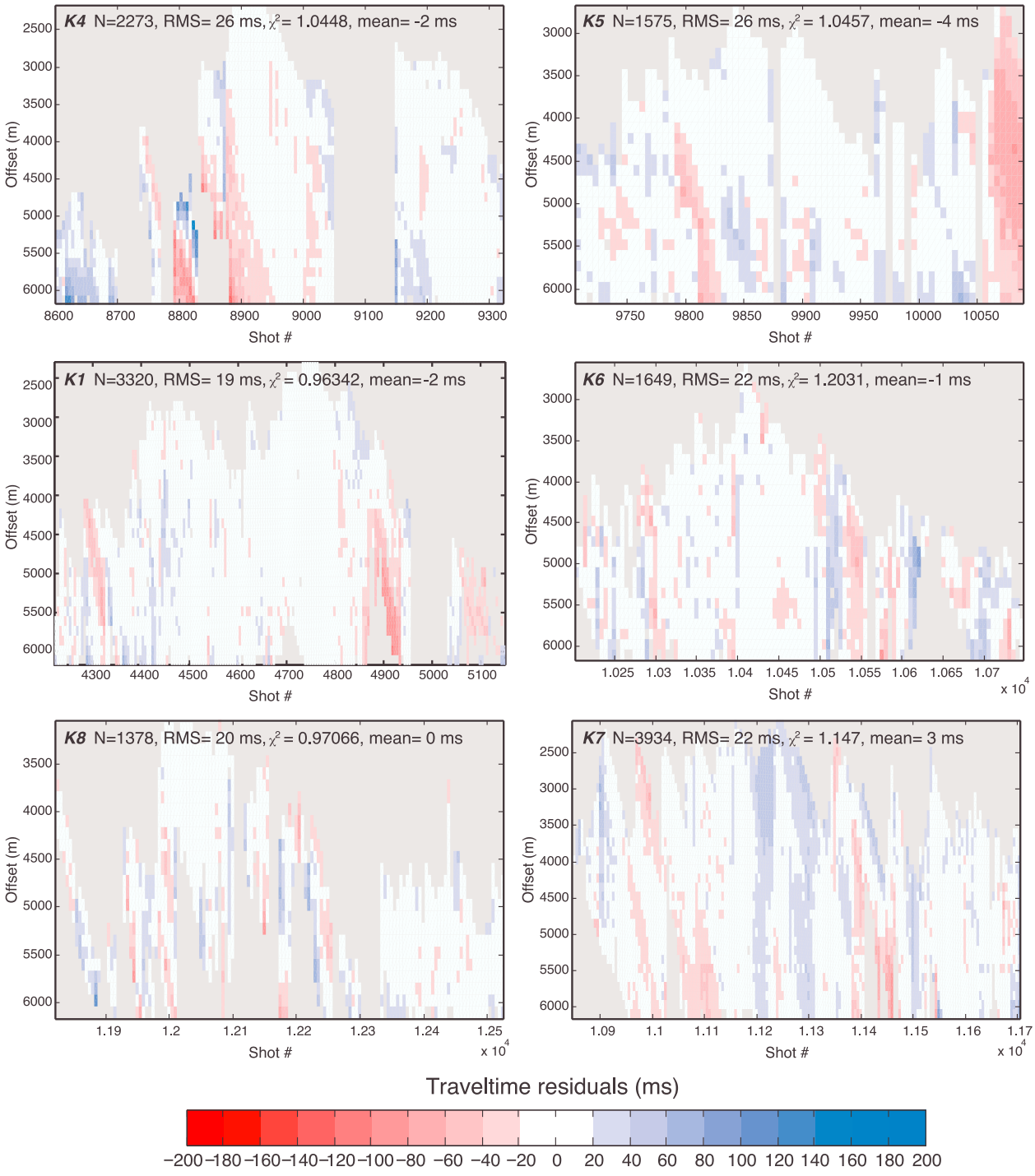

Figure 8. Color maps of traveltime residuals predicted from the final tomographic models (Figure 7) displayed as a function of shot number and source-receiver offset for each seismic profile. Color breaks are every 20 ms. All the other items are as explained in Figure 6.

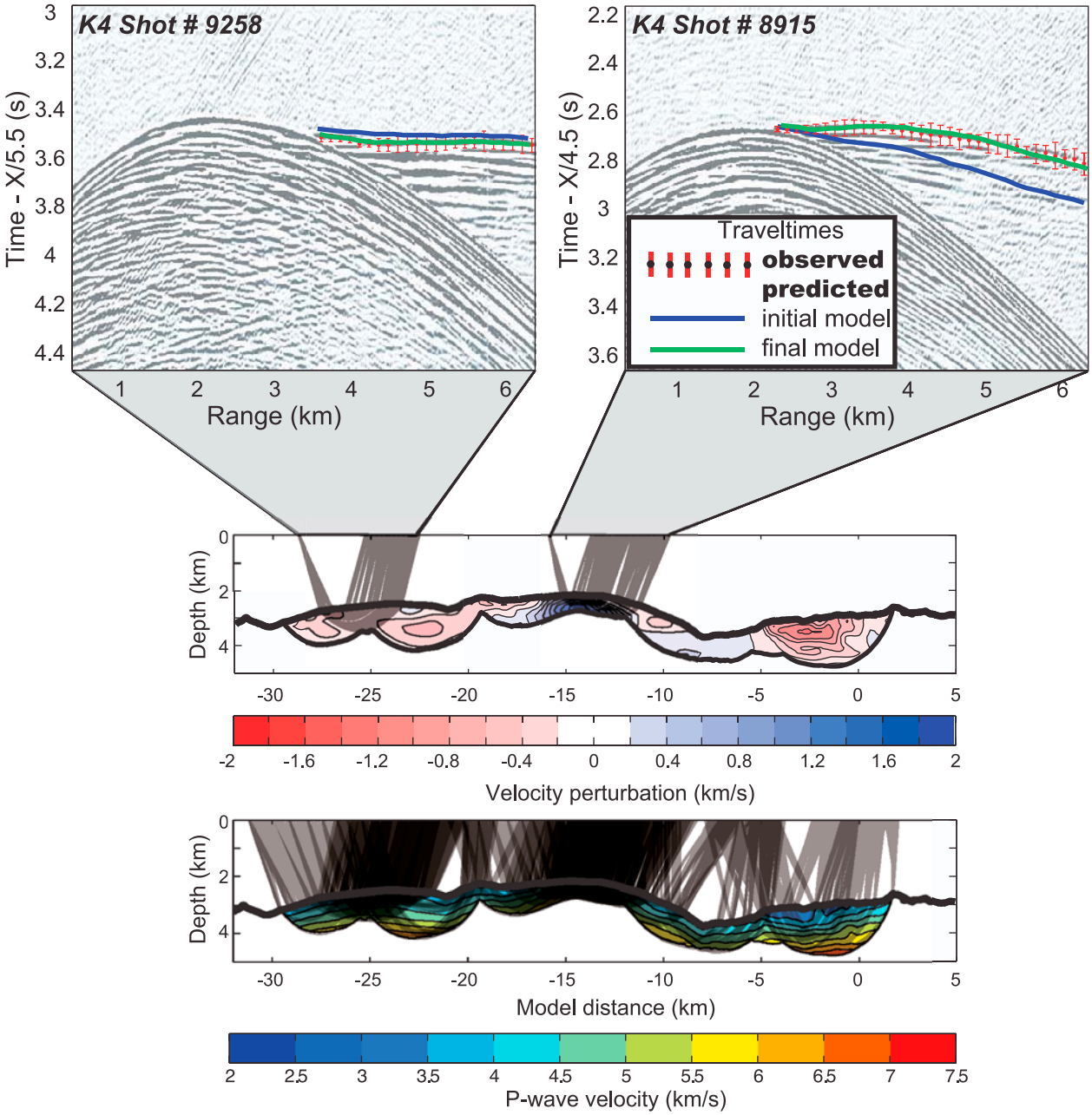

Figure 9. (top) Two representative shot gathers from profile K4 (Figure 2) with observed traveltimes and their assigned uncertainty (circles with red error bars). Traveltime curves are shown in blue as predicted by the initial model (Figure B1b) and in green as predicted by the final model (Figure 7). (middle) Final velocity model for profile K4, shown as perturbations with respect to the initial model, and contoured every 0.2 km s^{-1}. Raypaths (gray lines) for the two source-receiver pairs in Figure 9 (top) are shown. (bottom) Final velocity model for profile K4 with complete ray coverage and contours every 0.5 km s^{-1}.

areas of deeper seafloor that usually are sampled by fewer rays.

4. Seismic Tomography Results

[21] Our tomographic results show large lateral variations in *P* wave velocity structure in both strike and dip directions down to scales of 1 km or less within the upper ~0.5–2.0 km of the lithosphere across the Kane OCC (Figure 7). Velocities are greater than 3 km s^{-1} everywhere but rarely exceed 7 km s^{-1}. The lateral variations can be seen most easily by displaying the preferred velocity models relative to the initial 1-D model

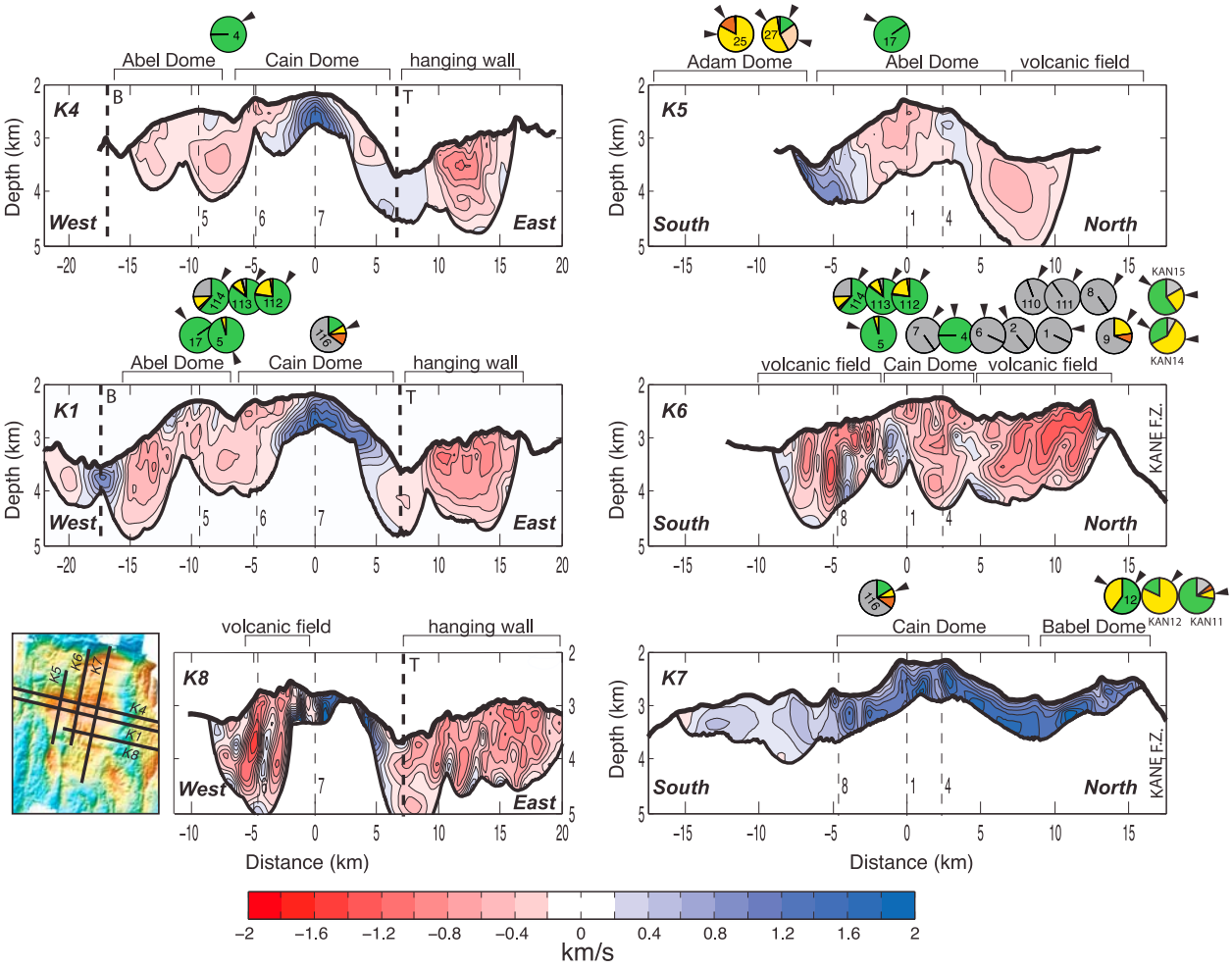

Figure 10. Final velocity models from Figure 7, here shown as perturbations with respect to the initial 1-D velocity model (Figure B1b) and contoured every 0.2 km s^{-1}. Rock types sampled from slide scar headwalls and high-angle fault scarps within ~2 km of the seismic profiles (larger pie diagrams in Figure 15) are shown above the profiles; small arrows on the pie diagrams indicate which rock types (color coded as in Figure 15) are known or reasonably interpreted to represent bedrock composition. The bottom left inset shows locations of the six seismic profiles on the Kane OCC.

(Figure 10). Lateral resolution tests (see section C1 and Figure C1) indicate that anomalies that are ~2.0 km wide and less than 0.5 km subseafloor can be trusted and interpreted, except at the ends of profiles where resolution is poorer.

[22] We use the *P* wave velocity models to calculate vertical velocity gradients over 200 m depth intervals along the profiles (Figure 11). We find that in the upper ~500 m velocity and vertical velocity gradient are positively correlated (Figure 12). This correlation allowed *Canales et al.* [2008] to define three broad classes of velocity structure in the shallow part of the basement beneath MAR OCCs (see section 2.1). Our results also fall into these three classes of velocity structure, which encompass almost all combinations of velocity and velocity gradient (Figures 7, 11, and 12): Class V1 occurs primarily in the hanging wall at the eastern ends of the dip lines and in the northern and southern parts of profile K6; class V2 is the most commonly observed velocity configuration, and it is prevalent over the terminations and in the western parts of the dip lines, over most of profile K5, in the central part of profile K6, and in the southern one third of profile K7; class V3 is observed in the central sections of the dip lines, the southern end of profile K5, and the northern two thirds of profile K7. The along-profile extents of V1, V2, and V3 velocity characteristics in the upper ~500 m of the tomographic models are

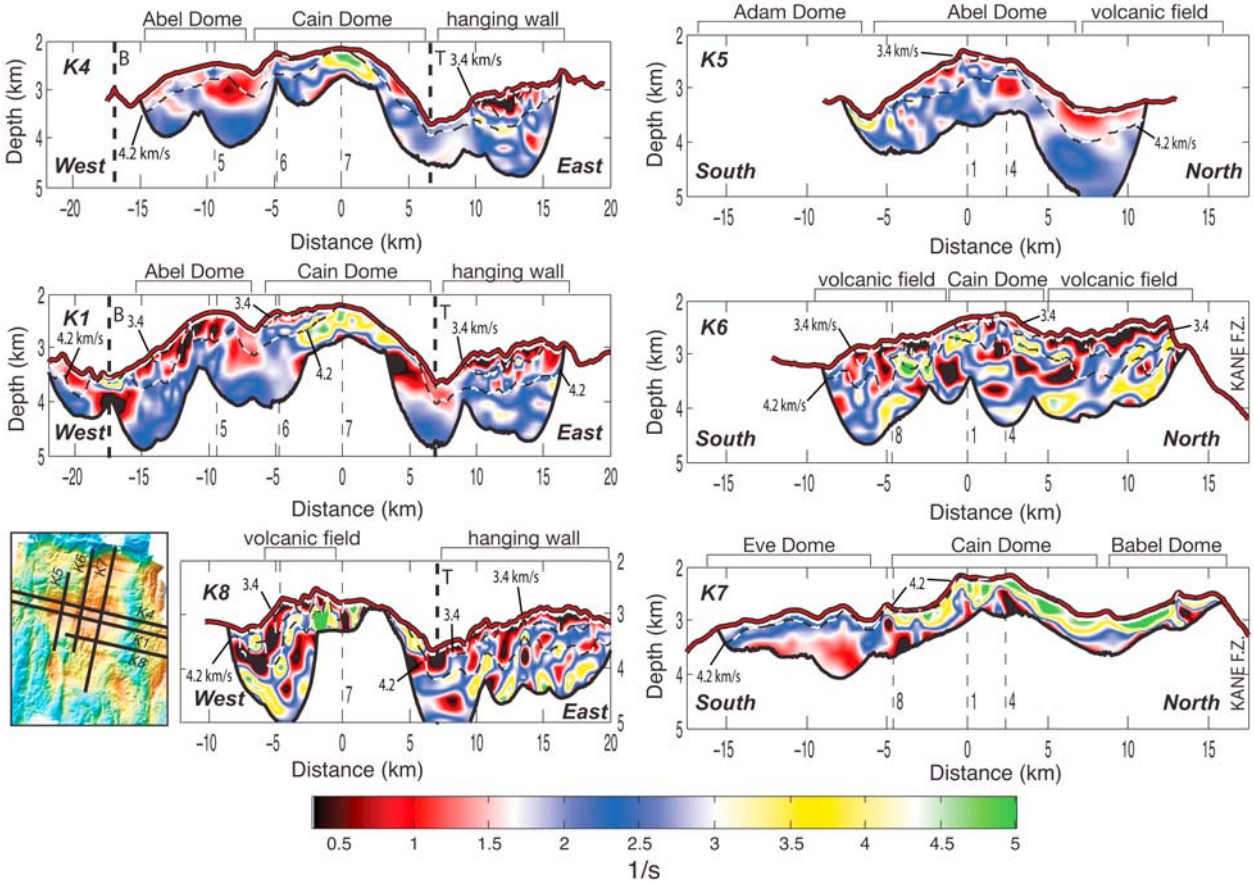

Figure 11. Vertical velocity gradient along the Kane profiles, calculated from the tomographic models of *P* wave velocity (Figure 7). Profile locations are indicated in the bottom left inset. Gradients were calculated in vertical windows at a grid spacing of 200 m (i.e., the grid spacing for tomographic inversions). The 3.4 km s^{-1} and 4.2 km s^{-1} isovelocity contours from Figure 7 are shown as dashed lines and are labeled. Morphological features are labeled at the top of the profiles.

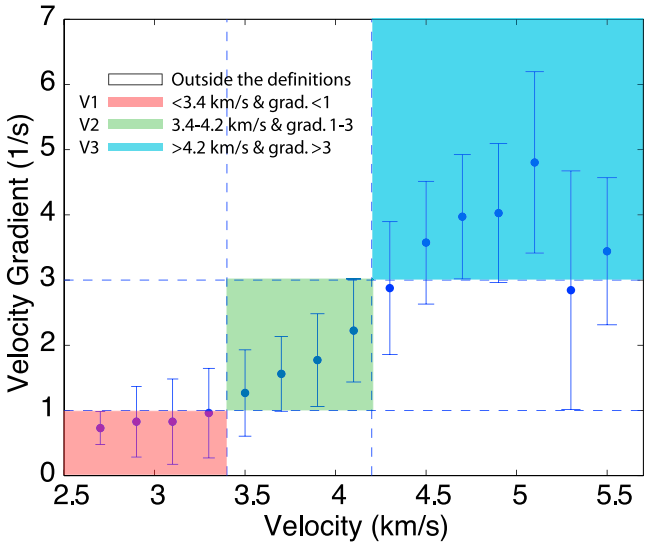

Figure 12. Correlation between the shallow (~500 m subseafloor) velocity and vertical velocity gradient structures. The data are binned in 0.2 km s^{-1} increments of the velocity. Vertical bars are one standard deviation of the average shallow vertical velocity gradient within each bin. Definitions of the three classes of velocity structures are indicated (same as in Figure 7; see section 4 for explanation).

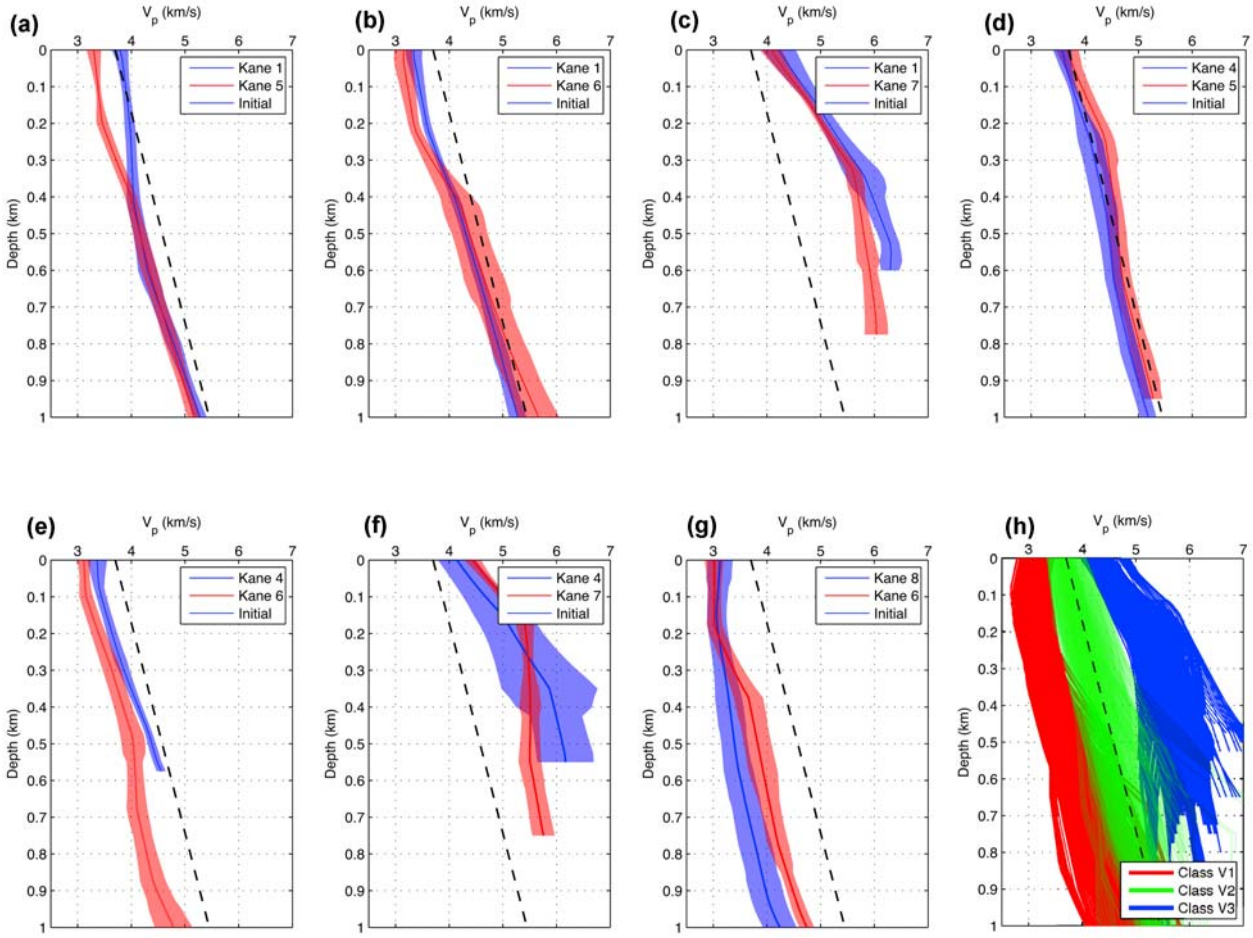

Figure 13. (a–g) Comparison of velocity-depth profiles at crossing points of dip and strike profiles (shown in blue and red, respectively). The shaded areas indicate $\pm 1\sigma$ velocity uncertainty (Figure 14). The initial average 1-D velocity model (Figure B1b) is shown by dashed lines. (h) Velocity-depth bands extracted from the six profiles within regions defined as class V1, V2, and V3.

indicated by color bars at the top of each profile in Figure 7.

4.1. Dip Lines (Profiles K4, K1, and K8)

[23] Patterns of velocity variations between the breakaway zone and the termination are very similar among the three dip line velocity models (Figures 7 and 10). Each model can be divided laterally into three zones: an eastern zone consisting of hanging wall terrain that has V1 structure; a central zone over the central and eastern sections of Cain Dome that is characterized by V3 structure; and a western zone over Abel Dome and the western side of Cain Dome that has V2 structure. The western end of profile K8 falls between Cain and Eve Domes (Figure 1) and crosses a possible volcanic field with V1 structure [*Dick et al.*, 2008]. At the western end of profile K1, there is a small high-velocity body present near the detachment breakaway (V3 structure).

4.2. Strike Lines (Profiles K5, K6, and K7)

[24] The velocity structure along the strike lines shows greater variability between lines (Figures 7 and 10). The central part of profile K5 crosses Abel Dome and stops at a possible volcanic field at its northern end. Most of the profile has V2 structure, but the southern end impinges on the northern part of Adam Dome and shows V3 structure.

[25] Profile K6 runs along the crest of the footwall at East Fault. V1 structure characterizes the northern one third of the profile where a volcanic ridge caps the crest of East Fault, and intermediate V2 structure is present in the central section. Mixed intermediate to low velocities and V1/V2 structure appear in the southern one third of the profile where volcanics appear to be present.

[26] The northern and central parts of profile K7 correspond to Babel Dome and the shallowest part of Cain Dome, respectively, and both exhibit V3

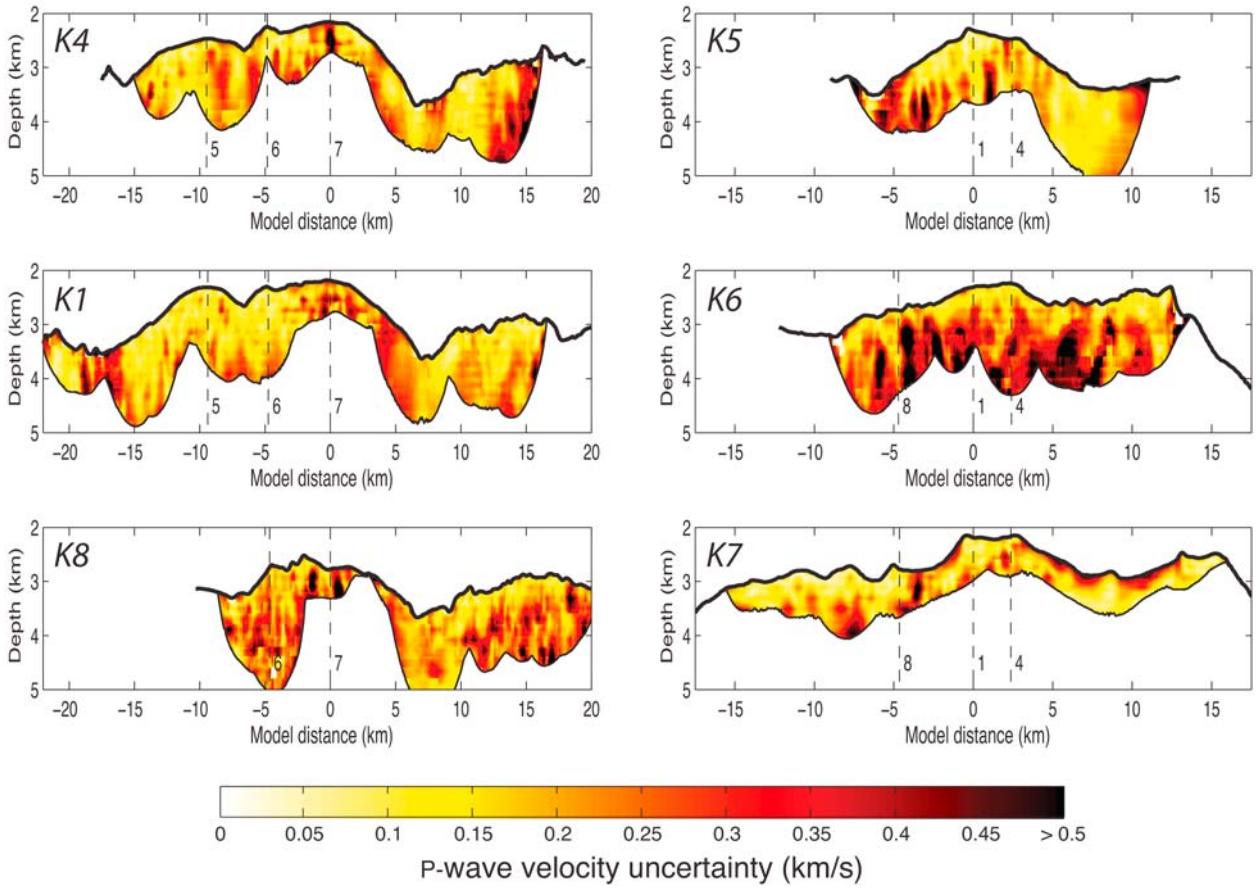

Figure 14. Results of *P* wave velocity uncertainty estimation. The bottom of all profiles is the maximum raypath depth of the corresponding final tomographic models (Figure 7). The estimated velocity uncertainty is approximated by the standard deviation of 100 Monte Carlo realizations. Note that the dominant velocity uncertainty is $\leq$0.3 km s^{-1}, although there are regions where the uncertainty can be as large as 0.4–0.5 km s^{-1} or even higher. Profile crossings are indicated by vertical dashed lines as in Figure 7.

structure. The southern part of profile K7 crosses a pair of domes east of Eve Dome, where intermediate V2 structure is present.

[27] Figure 13 compares velocity-depth profiles at intersection points of the strike lines and dip lines within the range of velocity uncertainties (Figure 14). Details of the velocity uncertainty estimation are given in section C2. With the exception of the structure at the intersection between profiles K1 and K5 in the upper 400 m, all of the other profiles agree with each other, considering the estimates of the velocity uncertainty (the locally large velocity uncertainty of profile K4 at its intersection with profile K7 is due to the inability of the modeling approach to accurately determine the magnitude of the high-velocity anomaly that characterizes this area (Figure 10)). Therefore we do not find in our results any convincing signal of seismic anisotropy that could be associated with aligned cracks [e.g., *Stephen*, 1981, 1985; *Dunn and Toomey*, 2001], mineral alignment, or lithology [e.g., *Miller and Christensen*, 1997; *Christensen*, 2004]. In places where intersecting profiles do not match, the discrepancy may be due, at least in part, to three-dimensional complexity and small-scale heterogeneity that cannot be captured and modeled with our 2-D approximations and assumptions.

5. Interpretation: Lithology-Velocity Correlation

[28] In this section, we use constraints provided by geological samples to interpret the seismic velocity structure of the Kane OCC in terms of dominant lithologies. We also use geological and seismic observations from other MAR OCCs [*Canales et al.*, 2008] to assist in this interpretation.

[29] The extensive suite of geological samples from the Kane OCC reported by *Dick et al.* [2008] and *Auzende et al.* [1994] (Figure 15) can

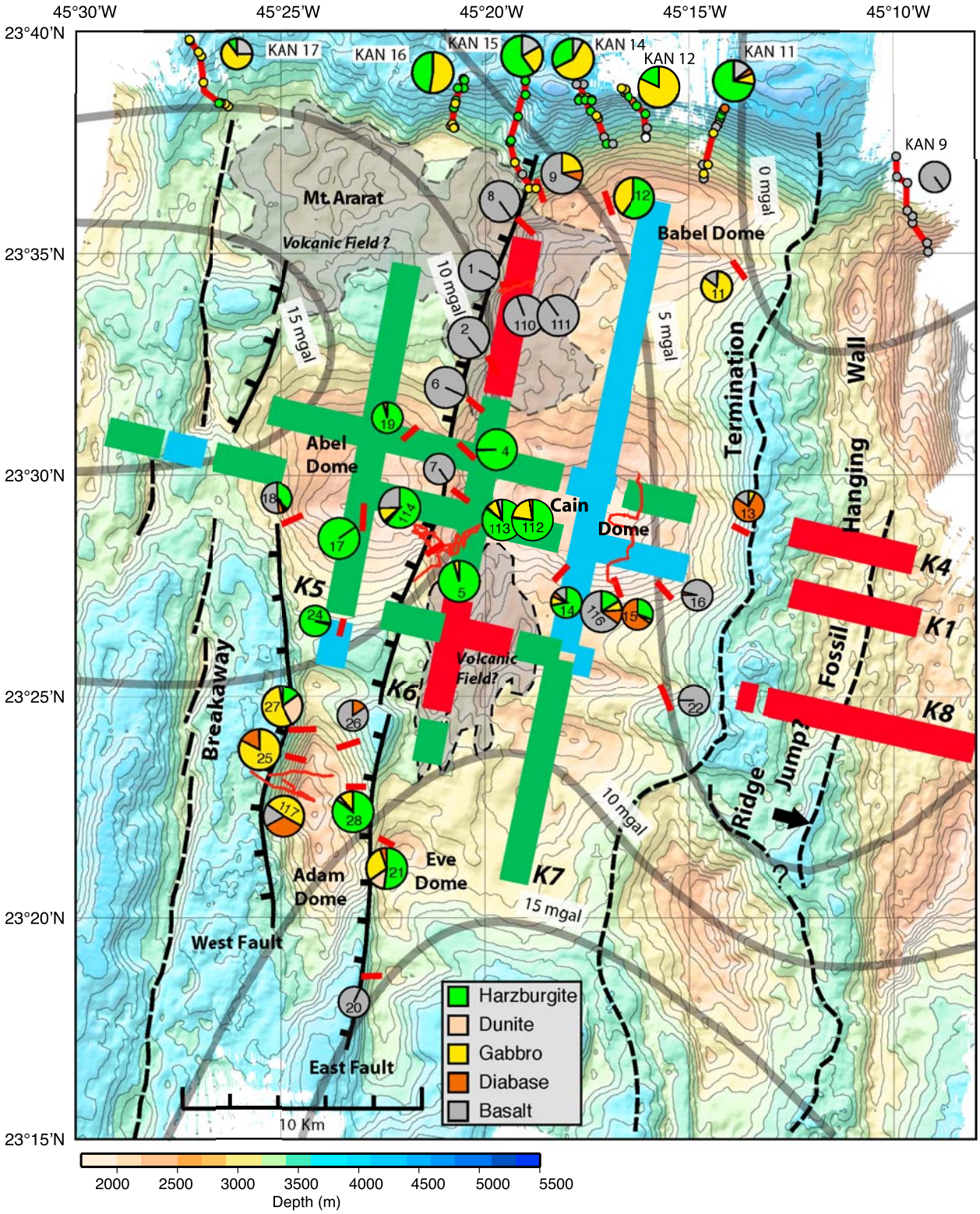
45°30'W
45°25'W
45°20'W
45°15'W
45°10'W
23°40'N
23°35'N
23°30'N
23°25'N
23°20'N
23°15'N
KAN 17
KAN 16
KAN 15
KAN 14
KAN 12
KAN 11
KAN 9
Mt. Ararat
Volcanic Field ?
Babel Dome
0 mgal
10 mgal
15 mgal
5 mgal
Termination
Wall
Hanging
Abel Dome
Cain Dome
K5
K4
K1
K8
K6
K7
Volcanic Field?
Fossil Ridge Jump?
Breakaway
Adam Dome
Eve Dome
West Fault
East Fault
Harzburgite
Dunite
Gabbro
Diabase
Basalt
10 Km
2000
2500
3000
3500
4000
4500
5000
5500
Depth (m)

Figure 15

be divided into (1) samples obtained from beneath the detachment surface on slide scar headwalls or high-angle fault scarps; (2) rock assemblages commonly associated with detachment shear zones, such as mylonites and serpentine schists, that may displaced along the fault and thus are not necessarily representative of the underlying bedrock; and (3) allochthonous debris clipped from the hanging wall or otherwise dispersed across the detachment surface. We rely here on the first type of samples, which consists of massive, partially serpentinized peridotites (Jason dives 112, 113, 114, dredges 4, 5, 12, 17, 21, 27, 28, and KANAUT dives 11, 14, 15 and 16), gabbros (Jason dives 116, 117, dredges 9, 12, 21, 25, 27, 28, and KANAUT dives 12, 14, 15 and 16), autochthonous pillow basalts (Jason dives 110, 111), and abundant pillow basalts obtained in dredges 1, 2, 6, 7, and 8 (Figure 15). In Figure 10, locations of bedrock samples are projected onto the seismic velocity profiles where the samples are within ~2 km of the profiles. This allows us to identify clear velocity-lithology correlations.

[30] The low velocities and velocity gradients (V1 structure) found along the northern part of profile K6 correlate systematically with pillow basalts that form a volcanic ridge along the crest of the footwall of East Fault in its northern part (Figures 7, 10, and 11). Comparable velocity structure occurs in the hanging wall on the three dip profiles. Although the hanging wall has not been sampled, it has irregular, hummocky morphology that is characteristic of volcanic terrain (Figures 1 and 15), and it therefore is likely to be dominantly volcanic rocks, possibly with sheeted dikes in the deeper part of the section. V1 structure is also found at the southern end of profile K6 and the western end of intersecting profile K8 where irregular, hummocky morphology suggests that a volcanic field is present [*Dick et al.*, 2008] (Figures 1 and 15). From all these correlations, it appears that portions of the profiles that are characterized by V1 structure represent dominantly volcanic rocks, plus or minus an uncertain component of underlying sheeted dikes.

[31] The mostly intermediate velocities and velocity gradients (V2 structure) across Abel Dome and the western part of Cain Dome correlate with massive outcrops of serpentinized peridotites (profiles K1, K5, and K6, Figures 7, 10, and 11). Thus we interpret these velocity characteristics to be associated dominantly with basement consisting of serpentinized peridotite.

[32] There are very few bedrock samples at the Kane OCC where class V3 dominates. However, the available samples support the interpretation of *Canales et al.* [2008] (based on drilling of 1415 m of gabbros at IODP Hole 1309D in Atlantis Massif OCC) that class V3 is associated primarily with gabbros (Figures 7, 10, and 11). V3 structure is prominent where profile K5 approaches Adam Dome, and both Jason dive samples and dredges show that this dome is dominantly gabbroic, with secondary sheeted dikes. Along profile K1, Jason Dive 116 sampled in-place, altered gabbros from basement exposed in a small scarp in the area of V3 structure over the crest of Cain Dome. At the northern ends of profiles K6 and K7, submersible samples from outcrops and dredge samples from scarps suggest a dominance of gabbros with lesser peridotites. Thus, we argue that the V3 structure observed beneath the crests of Babel and Cain Domes indicates a dominantly gabbroic composition, much as appears to be the case to the southwest at Adam Dome. One small body with V3 structure is located at the breakaway on profile K1; however, we do not know the along-isochron extent of this anomaly, and its size is at the limit of what we feel comfortable interpreting on the basis of our lateral resolution tests (see section C1 and Figure C1). Although the V3-gabbro correlation

Figure 15. Interpretation of upper basement composition along the Kane MCS profiles based on velocity characteristics (smoothed from Figure 7) and their lithologic correlations deduced in this paper. Along the profiles, red presents pillow basalts (±sheeted dikes), blue is dominantly gabbros, and green indicates serpentinized peridotites. Areas of significant size where velocity characteristics are uncertain (on the basis of the model assessment, Appendix C) are not included. Pie diagrams show lithologic proportions by weight of samples obtained from ROV/submersible dives and dredges on two cruises: KANAUT Expedition [*Auzende et al.*, 1994] and R/V *Knorr* cruise 180-2 [*Dick et al.*, 2008]; inset at bottom shows the key to lithology. The diagrams represent all samples including allochthonous debris. The larger pie diagrams show locations where at least part of the sample suite is known or is reasonably interpreted to represent true basement; see Figure 10 for identification of these samples, which are used to interpret velocity-lithology correlations. Tracks of Jason dives 110–117 and Nautile dives KAN 9–17 are shown in red; small colored circles along Nautile tracks show lithology at sample locations. Red bars locate dredge tracks. Gray contours are residual mantle Bouguer anomaly (RMBA) from *Maia and Gente* [1998]. Contour interval in the underlying bathymetry map is 100 m. Other features are as described in Figure 1.

appears to be good to a first order, we note that V3 zones may include other lithologies, notably peridotite, as indicated by rocks from dredge 12 and Nautile dives in the area of Babel Dome. Following this reasoning, it may be that some areas that have moderately elevated velocity but lack high-velocity gradient (e.g., the southern one third of profile K7, Figures 7, 10, and 11) could include a mixture of gabbros and serpentinized peridotites. Along the southern part of profile K6 (Figures 7 and 10), the more prominent differentiation of moderately high to moderately low velocities could similarly indicate interspersed peridotites, intrusives, and volcanics on scales of a few kilometers or less.

6. Discussion

6.1. Variations in Velocity Structure

[33] We have attributed observed lateral variations in velocity structure primarily to lithological composition, but other contributing factors are possible. For example, the observed variations in *P* wave velocity might be due to lateral changes in porosity within a single type of lithology [e.g., *Wilkens et al.*, 1991; *Berge et al.*, 1992]. In basalt saturated with pore fluid (brine), a velocity change of ~2 km s^{-1} (i.e., the average variation observed along our dip profiles, Figures 7 and 10) could be explained by ~3–15% change in porosity; this assumes a bulk modulus of 95.0 and 2.44 MPa, shear modulus of 42.0 and 0.0 MPa, densities of 3.0 and 1.023 g cm^{-3}, for matrix (basalt) and inclusions (brine), respectively, and an aspect ratio of the inclusions of 0.01–0.1 [*Kuster and Töksoz*, 1974]. Such variations in porosity are not unusual [e.g., *Wilkens et al.*, 1991], and they have been proposed to explain the documented increase in seismic velocity of the upper oceanic crust with age [*Houtz and Ewing*, 1976] as pore spaces are filled with mineral precipitates and alteration products [*Carlson and Herrick*, 1990; *Grevemeyer and Weigel*, 1997]. One might expect that changes in velocity due to fractures and alteration would show some correlation with tectonic context, with lower velocities expected near the presumably more tectonized northern end of the paleospreading segment bounding the Kane FZ than near the center of the segment [e.g., *Minshull et al.*, 1991; *Detrick et al.*, 1993; *Canales et al.*, 2000b]. However, we do not find clear evidence for this, as structure along strike profiles is more homogeneous than along dip profiles (Figure 10). Thus, we know of no reasonable explanation for how such lateral, multikilometer-scale porosity variations would develop in the Kane OCC basement if it were of uniform composition.

[34] If porosity changes do influence the observed seismic velocity structure, they most likely are closely linked to the lithological changes already described. For example, the velocity gradient found in the shallow part of areas characterized by V3 structure can be interpreted as resulting from a highly fractured thin uppermost layer of gabbros that has porosity rapidly decreasing with depth. This effect could also be present in serpentine-dominated areas characterized by V2 structure, although a significant degree of serpentinization would also reduce velocities so that the velocity gradient of class V2 is lower than in V3 regions.

[35] Are the velocity-lithology relationships that we have described reasonable? Although the elastic *P* wave velocities of intact, relatively unaltered, saturated samples of oceanic basalts range from approximately 5 to 6 km s^{-1} [*Johnson and Semyan*, 1994], *P* wave velocities of the uppermost oceanic crust measured in situ by seismic refraction are as low as 2.2 km s^{-1} at near-zero age [*Purdy and Detrick*, 1986; *Harding et al.*, 1989; *Vera et al.*, 1990]. Our V1 velocity class, assigned to basalts (±dikes), falls well within the range noted above. To a first order, observed velocities in the lower part of this range can be taken as a reasonable indicator of the presence of basalts rather than serpentinized peridotites and gabbros.

[36] For intact samples of gabbro and serpentinized peridotite cored from the MARK area, laboratory-measured *P* wave velocities at appropriate confining pressures range from 6.7 to 7.4 km s^{-1} for gabbros, and from 4.7 to 6.8 km s^{-1} for fully serpentinized and ~30%-serpentinized peridotite [*Miller and Christensen*, 1997]. These velocities are at the high end of the range of velocities that we observe at the Kane OCC. However, our refraction data sample large volumes of rock that are permeated by fractures and other porosity with varying geometry, so it is to be expected that the refraction velocities will be lower (perhaps significantly lower) than velocities measured on intact laboratory samples. This effect is clearly illustrated by velocity measurements of gabbros in the upper part of IODP Hole 1309D in the Atlantic Massif OCC, where meter-scale sonic log velocities and kilometer-scale refraction velocities are ~5–6 km s^{-1} [*Canales et al.*, 2008], much lower than the 6.7–7.4 km s^{-1} velocities measured on laboratory samples. It should be noted that the lack of solid-rock integrity at seismic scales probably can also

reduce velocities of serpentinized peridotites well into the range of basalt velocities; *Canales et al.* [2008] found that the upper part of the well sampled serpentinite edifice at the south edge of Atlantic Massif OCC produced refraction velocities of only ~3.5–4 km s^{-1}.

[37] The above considerations demonstrate that the velocity-lithology relationships we have proposed are entirely reasonable. However, it is also clear that refraction velocities do not uniquely define rock type in OCC settings, so it is important that the scales and limits of the correlations be tested by future sampling in as much detail as possible. Future constraints can also be imposed by independent parameters such as V_P/V_S ratio.

[38] Up to this point we have discussed lateral variations defined by apparently robust velocity, velocity gradient, and lithologic correlations within the upper ~0.5 km of the OCC. Vertical variations in the deeper record are more difficult to evaluate. To a first approximation, it seems reasonable to assume that areas with shallow V2 signature together with a low velocity gradient at deeper levels are likely to be peridotites with progressively decreasing serpentinization to the full depth of our observations. If this is correct, it implies that substantial serpentinization can occur to depths of at least 1.5 to 2 km. For example, observed 6 km s^{-1} velocities at 1.5 km depth below Abel Dome (Figure 7) would imply ~60–65% serpentinization, on the basis of the measurements of *Christensen* [2004]. Elsewhere, it also seems reasonable to interpret high-velocity, high-(vertical) gradient zones within this presumed "serpentinite matrix" as the upper margins of gabbro plutons, just as V3 characteristics correlate to gabbros in the shallow section. In this context, prominent, irregular deep structure, as for example in profile K6 at and south of Cain Dome, and beneath the hanging wall in profile K8, may indicate gabbro bodies with sizes on the order of ~2km or less (Figure 7).

6.2. Seafloor Morphology, Rock Samples, and Subseafloor Geology

[39] We observe a consistent and apparently robust correlation between subseafloor velocity characteristics and lithology of samples that are either documented, or highly likely, to be from intact basement outcrops along high-angle fault scarps and slide scars. These samples commonly represent only a small fraction of recovered rocks (Figure 15), which emphasizes the well known difficulty of interpreting basement composition from surficial rock assemblages, particularly those obtained in dredges. Seismic observations such as those reported here, constrained by bedrock lithology determined at high-angle fault scarps or slide scars, are potentially a very useful tool for assisting geological mapping outside the often very limited areas where bedrock sampling is possible.

[40] An important result of our analysis is that the morphology of individual domes on the Kane OCC cannot be uniquely associated with any particular lithology. For example, Abel and Cain Domes, although separated by East Fault, exhibit morphologic continuity in terms of shape, size, and style of corrugations, even though Abel Dome and western Cain Dome are predominantly serpentinized peridotite, whereas the central part of Cain Dome is dominantly gabbro. This morphologic continuity implies that, once established, the form of a detachment fault surface may be very persistent despite changes in pattern of magmatism.

6.3. Relation of Gravity Anomalies and Velocity Structure

[41] Gravity studies show elevated residual mantle Bouguer anomalies (RMBA) over most of the Kane OCC [*Morris and Detrick*, 1991; *Ballu et al.*, 1998; *Maia and Gente*, 1998], indicating relatively high lithospheric densities that are commonly interpreted as thinned crust [e.g., *Tucholke et al.*, 1998]. There is a reasonable correlation between seafloor sample lithology and RMBA pattern [*Cannat et al.*, 1995a; *Dick et al.*, 2008], and we find that the RMBA is also generally consistent with the subseafloor velocity structure (Figures 15 and 16). However, such correlations should be viewed with the caveat that RMBA represents lithospheric structure at much lower resolution and deeper levels than seafloor samples and shallow velocity structure do. Elevated RMBA occurs over Abel Dome to western Cain Dome where V2 velocity structure indicative of serpentinized peridotite predominates. Elevated RMBA also occurs over the southern part of the OCC both at and southeast of Eve Dome where moderate velocities (profile K7, Figure 7) might indicate a mixture of gabbros and peridotites. Reduced RMBA occurs over Babel Dome, the central to eastern parts of Cain Dome, and Adam Dome where there is geological evidence of gabbroic plutons, where V3 velocity structure occurs (Figure 15), and where the highest velocities generally are observed (Figure 16). The lowest RMBA occurs east of the detachment termination

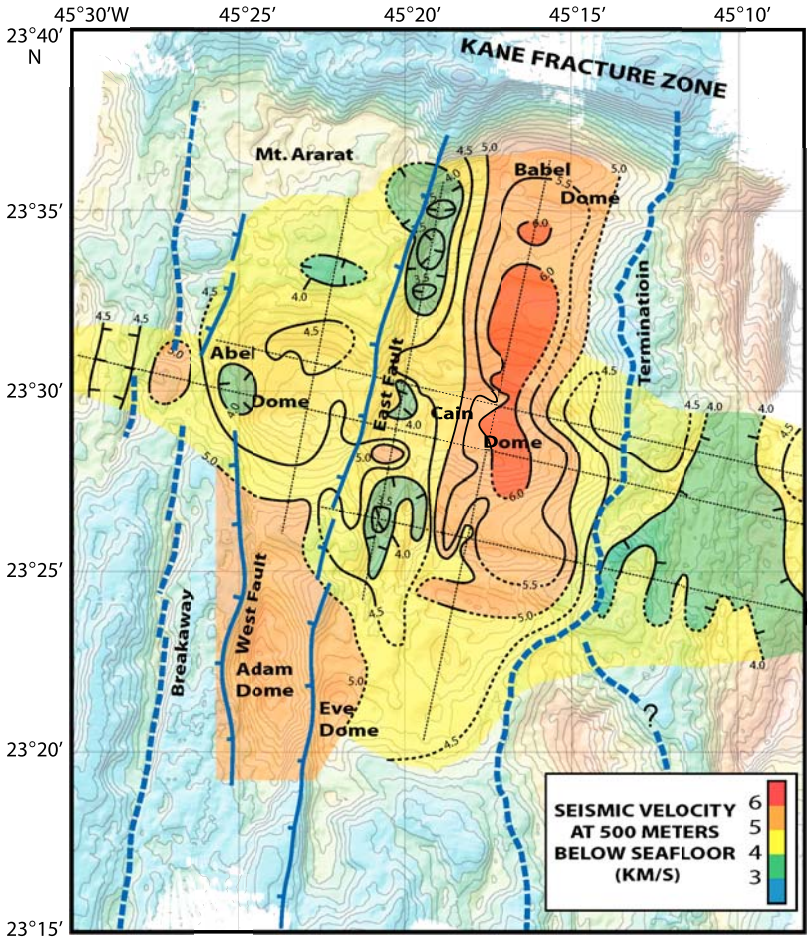

Figure 16. *P* wave isovelocity contours (interval 0.5 km s^{-1}) at 500 m below seafloor superimposed on bathymetry and simplified tectonic interpretation. Contours are dashed in unconstrained regions. Velocity in the area of Adam Dome is speculative and is inferred from gabbroic composition of basement demonstrated by geological sampling (Figure 15). Seismic profiles are shown as thin dotted lines.

over the volcanic hanging wall where V1 structure is present.

[42] Although the above correlation appears to be meaningful, it is the reverse of what would be expected in the V2 and V3 provinces (i.e., higher RMBA, and therefore higher density, such as is observed over exhumed mantle in the V2 region, would be expected to correlate with the highest velocities). This discrepancy may be explained by serpentinization of peridotites at shallow levels. Our seismic data only sample the uppermost lithosphere and therefore appear to be dominated by the velocity-reducing effects of this alteration, whereas unaltered, high-velocity mantle peridotite certainly lies at somewhat greater depths in the V2 region. The gravity effect of this deeper, high-density rock probably explains the elevated long-wavelength RMBA anomaly, despite the reduced density and velocity of serpentinized peridotite that is sampled at shallow levels. It will be necessary to achieve larger source-receiver offsets using either longer streamers or ocean bottom seismometers to resolve the depth of the transition to unaltered mantle.

6.4. Magmatism During the Evolution of Kane OCC

[43] Our lithological interpretation of the seismic profiles (Figure 15) indicates that there is marked variability in the shallow spatial distribution of gabbroic intrusions, serpentinized peridotites, and basalts over the Kane OCC at lateral scales of a few kilometers to >10 km. Here we discuss interpretation of magmatic conditions at the spreading axis as the Kane OCC formed and evolved. We note that our tomography models are only valid for the uppermost (<2 km) section of the lithosphere exhumed along the Kane detachment fault; there-

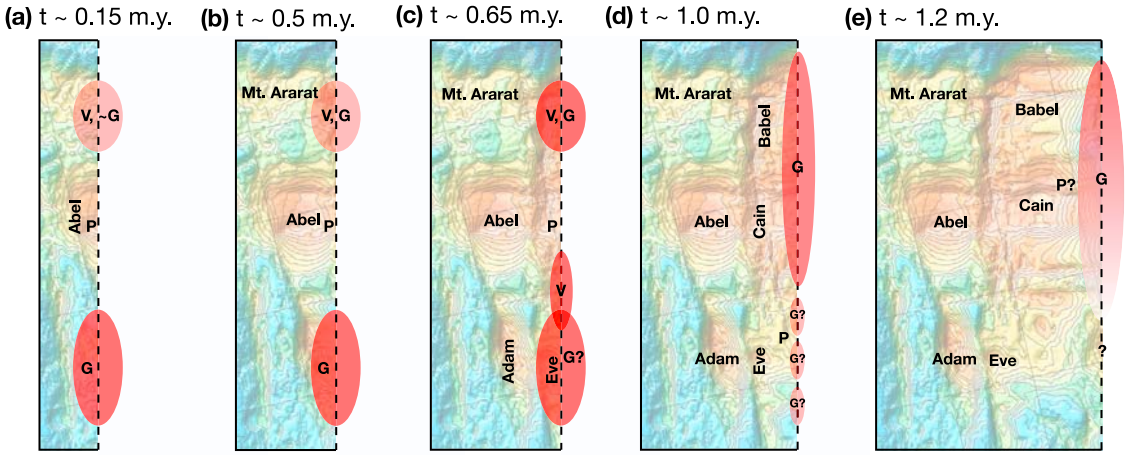

Figure 17. Schematic illustration of the temporal pattern of magmatism and/or exhumation of gabbro bodies during the evolution of the Kane OCC, inferred from lithological interpretation of the seismic profiles and basement samples (Figure 15) and from seafloor morphology. Note that the times of gabbro exposures are only minimum ages for emplacement because the gabbros could have been intruded many kilometers below the spreading axis. Plots show times following initiation of the Kane detachment fault. V and G refer to volcanics and gabbro, respectively, and P indicates peridotite. Pink and red ellipses indicate weaker and stronger magmatism that affected the footwall. See section 6.4 for discussion.

fore the following interpretation assumes that relative lateral changes in intrusive activity (or lack thereof) deeper in the lithosphere are similar to those inferred from the structure of the shallow lithosphere, an assumption that may not be valid if a significant proportion of melt is retained in mantle [e.g., *Lizarralde et al.*, 2004]. Also, we assume that lateral (i.e., temporal and spatial) changes in magmatism represent variations in melt supply to the ridge axis, but they could also represent changes in the efficiency of melt extraction from the mantle.

[44] We include interpretations made by *Dick et al.* [2008] based on geological sampling, particularly where we lack seismic constraints. Most importantly, our results allow us to expand the model of *Dick et al.* [2008] to areas where we have good seismic coverage but where there is limited geological sampling of bedrock in the footwall; this is particularly helpful for the younger (i.e., eastern) parts of the Kane OCC where sampling is limited to fault-rock assemblages and allochthonous debris scattered across the detachment surface (Figure 15).

[45] It is important to note that the time of exhumation of the plutonic igneous rocks at the seafloor gives only a minimum age for their intrusion because they could have been emplaced at a significant depth beneath the spreading axis [e.g., *Schwartz et al.*, 2005; *Grimes et al.*, 2008]. Conversely, the age of the lithosphere on which volcanics appear provides a maximum age for those rocks, which could have been extruded at any time after that lithosphere was exhumed.

6.4.1. Early Stages of OCC Formation

[46] The detachment fault that exhumed the Kane OCC initiated at ~3.3 Ma. Along the northern 2/3 of the enclosing spreading segment, this fault formed the western wall of the MAR rift valley and probably constituted the sole plate boundary while the OCC was being emplaced. Results from dip profiles K1 and K4 indicate that exhumation of peridotite commenced within ~2 km of the breakaway in the central part of the OCC as Abel Dome was being formed (Figure 15), although a narrow high-velocity zone at the breakaway in profile K1 might represent a small gabbroic body there (Figure 7). Thus this part of the Kane detachment fault initially cut through thin crust and to an uncertain depth into mantle in an area that had been experiencing relatively low magma supply (Figure 17a).

[47] To the north of Abel Dome we have no seismic control along strike near the breakaway zone, but samples from the southern wall of the Kane TF suggest that gabbros at least several hundred meters thick are present below the likely volcanic carapace of Mt. Ararat [*Auzende et al.*, 1994; *Dick et al.*, 2008] (Figures 15 and 17a). To the south of Abel Dome, geological samples [*Dick et al.*, 2008] and the southern end of profile K5

also indicate that robust magmatism emplaced gabbros beneath Adam Dome within ~4 km of the breakaway. Thus both north and south of Abel Dome the detachment fault appears to have reached gabbros at relatively shallow depths, which resulted in early exhumation of these rocks.

[48] Exhumation of peridotites continued for ~0.5–0.65 Myr in the central part of Kane OCC as Abel Dome and the western side of Cain Dome were emplaced (Figures 17b and 17c). Exhumed magmatic sections during this period remained focused at centers to the south in the area of Adam and Eve Domes and probably to the north in the area of Mt. Ararat. Corresponding bathymetric highs in volcanic, conjugate crust substantiate the interpretation that these were magmatically active zones [*Dick et al.*, 2008]. In the northern area, magmatism appears to have increased about ~0.65 Myr after breakaway, producing thick gabbro sequences that begin near East Fault and are exposed along the northern side of Babel Dome [*Dick et al.*, 2008] (Figure 17c).

[49] Although it is possible that there was robust magmatism in the intervening area of Abel and Cain Domes where peridotites have been sampled, but that the igneous section was removed in the hanging wall, this seems unlikely for two reasons. First, conjugate crust on the east flank of the MAR has deeper bathymetry in this zone, which suggests more limited magmatism. Second, this scenario would require that the detachment rooted below the gabbro-peridotite transition in the area of Cain and Abel Domes; thus, gabbro remnants from the hanging wall should be scattered across the exposed detachment fault surface, but this is not observed [*Dick et al.*, 2008]. To resolve this question more fully, it will be necessary to obtain seismic constraints on conjugate crust on the African plate.

6.4.2. Late Stages of OCC Formation

[50] The lithosphere that was exhumed about 1.0 Myr after breakaway shows a significant change in the distribution of magmatic crust, relative to the distribution of gabbro bodies observed in areas exhumed prior to that time (Figure 17d). Lithosphere of Babel Dome was affected by robust magmatism, as indicated by V3 seismic structure that we interpret as representing gabbro plutons along the northern part of profile K7 (Figures 7 and 15). However, the same structure occurs along strike to the south, which indicates that similar magmatism affected lithosphere exhumed in the central part of Cain Dome (Figure 16). It is uncertain whether the large along-strike extent of this zone (20+ km) resulted from southward propagation of magma from Babel Dome, or whether a separate magmatic center at Cain Dome became linked to that of Babel Dome (Figure 17d).

[51] Significantly lower (albeit still relatively high) velocities are associated with V2 velocity structure farther south along profile K7 to the east of Eve Dome (Figure 7). We suggest that these may be a mixture of gabbros and serpentinized peridotites, which implies that magmatism affecting the lithosphere exhumed in this area was reduced compared to that both to the north and at the older Adam Dome.

[52] Velocity characteristics in the youngest part of the footwall, ~2.2–2.1 Ma, may revert to V2 structure in the dip lines over Cain Dome and the saddle to the south of the dome (Figure 7), although this is uncertain because lateral resolution is decreased (Figure C1) and velocity uncertainty (Figure 14) is increased in this zone. If V2 structure is indeed present there, it suggests that the last lithosphere exhumed in the central part of the Kane OCC was not affected by significant magmatism and that serpentinized peridotite was once again being unroofed there (Figure 17e). We have no velocity control to the north of the youngest part of Cain Dome, but samples from KAN dive 11 along the northeast margin of Babel Dome imply that that part of the footwall continued to be intruded by gabbros [*Dick et al.*, 2008]. There are no velocity or sample constraints for the last part of the footwall exhumed to the south of Cain Dome.

[53] The detachment fault that exhumed the Kane OCC was abandoned at about 2.1 Ma when an eastward "ridge jump" occurred, i.e., when a new normal fault formed farther into the rift valley and captured a segment of the hanging wall from the African plate. The distance over which this jump occurred is unclear from available magnetic data, but it probably captured at least 4–5 km of the hanging wall in the dip direction (Figure 1). The distribution of depth along this captured hanging wall provides further insight into the along-strike state of magmatism in the last stage of OCC exhumation, and it appears to be consistent with observations noted above. The hanging wall is elevated adjacent to Babel Dome which, as noted above, appears to have been affected by late stage magmatism. In contrast, the hanging wall is deeper adjacent to Cain Dome where peridotite may have been last exhumed. The southern 1/3 of the fossil

hanging wall is still deeper; this could indicate that the nearby footwall was devoid of magmatic products, although there is an intervening large edifice at 23°20′N, 45°15′W that presently is unexplained, and this makes such an interpretation uncertain.

[54] It is commonly presumed that at slow spreading segments melt delivery from the mantle is focused at segment centers [*Whitehead et al.*, 1984]. While this may be the norm in many cases [*Lin et al.*, 1990], the compositional heterogeneity that we document across the Kane OCC demonstrates that there was strong spatial and temporal variability in magmatism along at least 2/3 of the northern MARK segment, and at least within the shallow lithosphere (~0.5–2.0 km). The variability occurs at spatial scales of less than a few kilometers to >10 km and at temporal scales of several hundred thousand years. Notwithstanding the spatial (lateral and vertical) limitations of our study, our results therefore suggest that magmatism was not focused at the segment center, and at times it was most robust at the northern segment end near the cold transform wall where magma supply commonly is thought to be limited [e.g., *Cannat et al.*, 1995a].

6.4.3. Surficial Volcanism

[55] Hummocky seafloor morphology typical of volcanic terrain is observed in the area of Mt. Ararat and eastward to the northern part of East Fault, as well as around East Fault to the south of Cain Dome (Figure 1). Jason dives along the northern part of East fault show that this morphology correlates with in situ pillow basalts [*Dick et al.*, 2008]. The time at which these volcanics were emplaced is unclear, but their spatial association with East Fault suggests that the magma was extruded along the fault during exhumation of the detachment footwall [*Dick et al.*, 2008]. Rotation of the footwall can result in bending-related normal faulting, with compression in lower part of the plate and extension in upper part, and this stress differential could force melts from the lower part into the upper part of the footwall [*Tucholke et al.*, 2001]. The low velocities observed along the northern part of East Fault in profile K6 indicate that the basalts emplaced there may have a thickness of a kilometer or more (Figure 7). The region of low velocities thickens toward the northern end of the profile, suggesting that the most extensive magmatism was near the transform wall; this is consistent with the development or enhancement of a northern magmatic center beginning ~0.65 Myr after breakaway (Figures 17c and 17d).

6.5. Implications for the Origin and Evolution of OCCs

[56] The recovery of predominantly gabbros in three deep holes thus far drilled in OCCs [*Dick et al.*, 2000; *Kelemen et al.*, 2004; *Blackman et al.*, 2006] and the consistent presence of gabbros near the termination of the Kane, Atlantis Massif, and Dante's Domes OCCs inferred from velocity models [*Canales et al.*, 2008] indicates that understanding the origin of the gabbro plutons is a key step toward understanding how OCCs form and evolve [*Ildefonse et al.*, 2007]. *Canales et al.* [2008] discussed three possible scenarios:

[57] 1. Detachment faulting was initiated by intrusions. A detachment fault may nucleate at depth where strain localizes around the margins of gabbro plutons intruded into peridotite [*Ildefonse et al.*, 2007; *Tucholke et al.*, 2008].

[58] 2. Intrusions were stimulated by detachment faulting. Following initiation of the detachment, intrusion of the plutons was stimulated, or enhanced, by decompression melting in the rapidly exhuming footwall.

[59] 3. Detachment faulting and intrusions are independent. The gabbros were intruded into the footwall as it was exhumed because of natural variability in the magmatic cycle (or variations in mantle fertility).

[60] Our detailed study of the Kane OCC provides some constraints on the first two hypotheses.

[61] In the first scenario, sufficient slip on the detachment may eventually exhume the gabbro pluton around which the fault nucleated. In the instance of the Kane OCC, the distance from breakaway to the gabbros ranges between about 12 and 18 km, depending on where the gabbro margins are defined in the velocity models along our dip lines (Figure 7). Therefore if the detachment initially dipped at ~45° (a reasonable dip according to Andersonian fault theory), it would have had to cut to ~10–13 km depth to reach the gabbros. If the fault dipped more steeply it would have to cut to greater depth.

[62] Microearthquake studies along the MAR axis [*Toomey et al.*, 1988; *Kong et al.*, 1992; *deMartin et al.*, 2007] indicate that detected seismicity extends only to ~7–8 km subseafloor depth, shallower than the above projected depth for the Kane detachment. However, the microearthquake studies are only short-term samples of longer-term brittle deformation of the lithosphere, and it may be

that long-term brittle deformation extends to greater depths. It is also possible that deep deformation associated with a detachment is largely ductile and thus is aseismic. Thus the idea that the Kane detachment nucleated on deep gabbro plutons in the mantle is not unreasonable.

[63] In the second scenario, the resultant unloading of the footwall as it was rapidly exhumed at the full spreading rate of ~23 mm/a, together with increased advection of heat [*Tucholke et al.*, 2008], may have stimulated decompression melting within the footwall [*Canales et al.*, 2008]. The possibility that serpentinized peridotite (V2 velocity structure) is present in the youngest part of the Kane OCC (dip lines K1, K4 and K8, Figures 7 and 15) would seem to argue against this mechanism, because we might expect that such melting would persist until the Kane detachment was finally abandoned. However, it is possible that refractory mantle was exhumed during the last stage of OCC formation and thus that melt generation was attenuated.

[64] At present, it is difficult to determine which of the above scenarios (or combination thereof) best explains the distribution of gabbros in the Kane OCC. Three kinds of future studies will provide important constraints. First, more complete coverage of seismic data, particularly near the breakaway, will help to resolve the distribution of likely gabbro bodies and thus determine the potential that the Kane detachment initially nucleated on deep intrusions. Second, age data on zircons in gabbros sampled from the footwall will help constrain the time at which the intrusions were emplaced, relative to the time of exhumation [e.g., *Baines et al.*, 2008; *Grimes et al.*, 2008]. Finally, drilling to obtain samples of peridotite from below the detachment shear zone will help to resolve questions about the fertility of the mantle that was exhumed in the footwall.

[65] Uninterrupted dip of Kane OCC surface corrugations at the contact with the hummocky fossil hanging wall shows that termination of slip on the detachment was accomplished by an eastward jump of the plate boundary (Figure 1). Reduced RMBA gravity east of the termination indicates that crust is thicker there, so there presumably was increased magmatism and heat in the axial lithosphere that stimulated the jump and the abandonment of the Kane detachment fault [*Canales et al.*, 2008]. By considering maximum and minimum ages for emplacement of the gabbro body under Cain Dome, we can place bounds on the time interval between that emplacement and the renewed magmatism and ridge jump at ~2.1 Ma. The earliest emplacement of the Cain gabbros would have been at 3.3 Ma (scenario 1, above), and the latest possible emplacement would have been when the western edge of the gabbros began to be exhumed from beneath the hanging wall, ~2.5 Ma. Thus the interval between the two magmatic pulses was at least 0.4 Myr but less than 1.2 Myr, although it most likely was in the higher part of the range (i.e., the Cain Dome gabbros were intruded when the footwall was well beneath the hanging wall).

7. Conclusions

[66] On the basis of interpretation of our seismic velocity models in conjunction with geological samples from the Kane OCC basement, we make the following conclusions.

[67] 1. We have successfully acquired and modeled long-offset MCS data over the relatively smooth and shallow surface of Kane OCC and have demonstrated that velocity structure can be reasonably correlated to basement lithology where appropriate in situ samples are available. This indicates that multichannel seismic reflection/refraction with a long streamer can be a powerful tool to constrain the shallow distribution of dominant lithologies within oceanic core complexes.

[68] 2. Two-dimensional traveltime tomography models reveal significant lateral variations in *P* wave velocity within the upper ~0.5–2.0 km of the lithosphere beneath the Kane OCC. The variations correlate to first order with lithologic variations in basement documented by in situ basement samples. With very limited exceptions, observed velocity characteristics fall into three categories: V1, low near-seafloor velocities (<3.4 km s^{-1}) and vertical velocity gradients (<~1 s^{-1}) at shallow levels; V2, intermediate shallow velocities (~3.4–4.2 km s^{-1}) and velocity gradients (1–3 s^{-1}); and V3, high shallow velocities (>4.2 km s^{-1}) and velocity gradients (>3 s^{-1}). Correlation with basement samples suggests that these velocity characteristics correlate predominantly with volcanics (±sheeted dikes), serpentinized peridotite, and gabbro, respectively. The observed distribution of V2 characteristics implies that serpentinization can extend deeply (>1.5 km) into the mantle.

[69] 3. The large-scale corrugated morphology that defines domes on the Kane OCC is not a good indicator of dominant basement lithology. A prime example is Abel and Cain domes, which are nearly

identical morphologically and lie in tandem along the same detachment slip line, but which have very different seismic structures that are representative of serpentinized peridotites and gabbros.

[70] 4. The detachment fault that formed the Kane OCC initiated at ~3.3 Ma and terminated at ~2.1 Ma. Within the exhumed footwall the velocity/lithology data document heterogeneous distribution of gabbroic intrusions, serpentinized peridotites, and volcanics at lateral scales of several kilometers to >10 km. Magmatism was not focused at the center of the enclosing spreading segment, as has been interpreted for some slow spreading ridge segments [*Dick et al.*, 2008].

[71] 5. Magmatism initially affected the northern and southern parts of the Kane OCC, while peridotites were exhumed in the central section. Within about 1 Myr after detachment faulting initiated, extensive gabbros were exhumed in the central to northern part of the OCC, with the southern part apparently affected by an intermediate level of magmatism. Within the last ~0.2 Myr of OCC formation, gabbros probably continued to be exhumed in the northern section up to the Kane transform wall, but peridotites probably were again exhumed in the central section; composition of basement in the southern part of the OCC at this time is uncertain.

[72] 6. A major, west facing high-angle normal fault (East fault) cuts the detachment surface along-isochron in the center of the Kane OCC and is associated with low seismic velocities and velocity gradients representative of volcanic rocks. We suggest that extrusion of the volcanics was facilitated by the stress differential between the upper and lower parts of the bending footwall as it was exhumed.

Appendix A: Details of Data Acquisition

[73] The seismic data employed in this study were recorded on a 6-km-long, 480-channel Syntron digital hydrophone streamer towed at a nominal depth of 10 m. Hydrophone group (i.e., receiver) spacing along the streamer was 12.5 m. The seismic source was a 10-element tuned air gun array with a total volume of 51L (3100 in^3) triggered by distance every 37.5 m and towed at a nominal depth of 8 m. Data were recorded in 10-s long records at a sampling rate of 4 ms. Positions of sources and receivers were derived from shipboard and tail buoy GPS receivers and compass-enhanced DigiCourse birds placed along the streamer.

Appendix B: Selecting a Starting Model and Inversion Parameters

[74] Figure B1a shows an example of how we selected the starting model for profile K4. First we calculated traveltimes for different starting models, with seafloor velocities ranging from 2 to 6 km s^{-1} at 0.2 km s^{-1} intervals, and vertical velocity gradients ranging from 0.5 to 3 s^{-1} at 0.25 s^{-1} intervals, and we identified the pair of parameters resulting in the lowest χ^2. Then we refined our starting model search in the vicinity of these parameters using a narrower range of seafloor velocities and vertical velocity gradients and chose the best 1-D model as the one that resulted in the smallest χ^2 (Figure B1a). The best 1-D models for all lines are shown in Figure B1b. All of the best 1-D models are similar to one another except for profile K7, which shows much higher seafloor velocity than the other five profiles. To make our results easier to compare between lines, we chose the average of the six best 1-D models as our preferred starting model for all six lines (Figure B1b). This averaged starting model has a velocity of 3.7 km s^{-1} at the seafloor and a vertical gradient of 1.75 s^{-1}; this is referred to simply as the starting model.

[75] To find the optimal inversion parameters for each profile, we ran inversions with different values of the damping parameter λ and calculated after each iteration the χ^2 for individual profiles (Figure B2). We selected the damping parameter λ as the one resulting in χ^2 as close as possible to 1.1 with the least number of iterations. After two iterations, profiles K1 (λ = 10), K4 (λ = 18), K5 (λ = 18) and K7 (λ = 30) achieve an acceptable statistical fit to the data, while data from profiles K6 and K8 (λ = 6) can be statistically fit after four iterations. For vertical smoothing we used s_z = 0.075 in all of the inversions; results were not significantly sensitive to values of $s_z < 0.075$, while larger s_z values resulted in large χ^2 misfits.

Appendix C: Model Assessment

C1. Lateral Resolution Tests

[76] The ability of the data to resolve lateral velocity variations can be assessed by performing corrugation tests [e.g., *Calvert et al.*, 2003; *Zelt et*

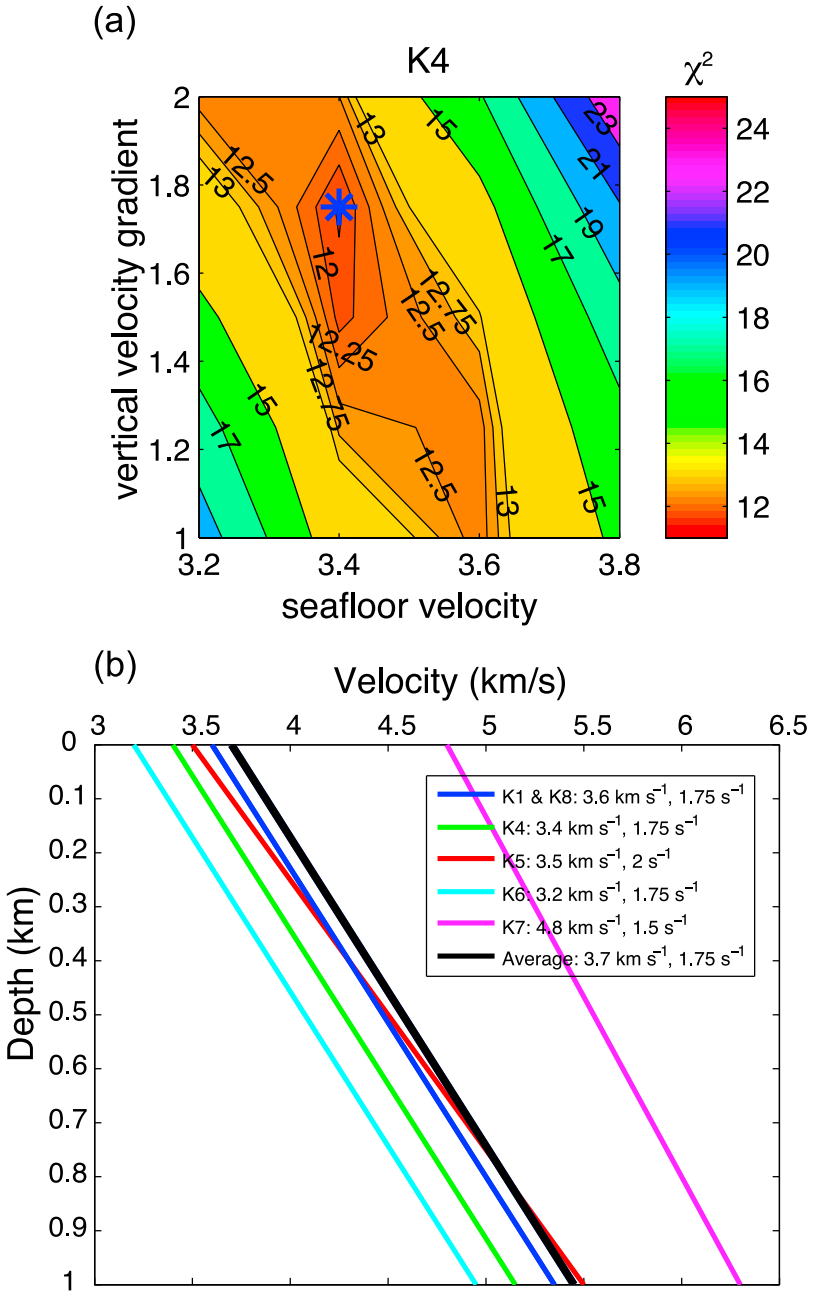

Figure B1. (a) Contour of traveltime residuals χ^2 (after one iteration) calculated for profile K4 using different seafloor velocities and vertical velocity gradients. The asterisk shows the best starting model that minimizes the traveltime residuals. (b) Best starting models for all six profiles are shown by colored lines, with the average model used for tomographic inversions shown in black. Note that all the best starting models are similar except for profile k7, which shows much higher seafloor velocity than the other profiles.

al., 2004], which are the 1-D equivalent of 2-D checkerboard tests commonly used in tomographic problems [*Zelt and Barton*, 1998]. In the corrugation test, a velocity anomaly pattern consisting of fixed width, vertical columns of alternating positive and negative anomalies were added to the initial model (Figure B1b) to create a perturbed velocity model. We varied the amplitude of the anomalies laterally by ±0.5 km s^{-1}, following a sinusoidal function. Synthetic first-arrival traveltime data were generated using the perturbed velocity model and the same source-receiver geometry as for the real data. We added random Gaussian noise to the synthetic traveltime gradients, $N(0, \sigma =$ 30 ms km^{-1}), following the method of *Zhang and Toksöz* [1998]. The synthetic data were then

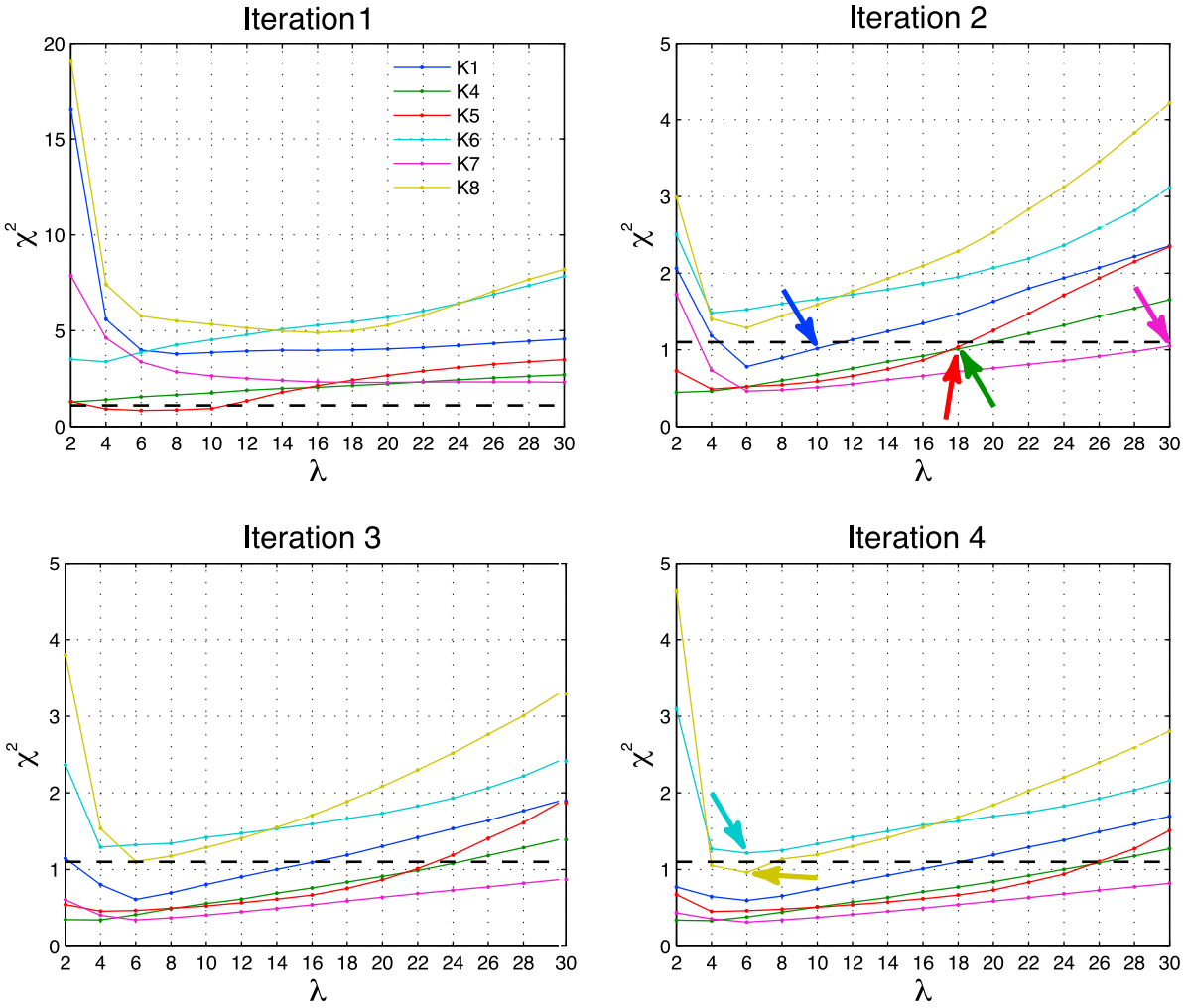

Figure B2. Variation in misfit function χ^2 between observed and predicted traveltimes as a function of damping parameter λ, for four inversion iterations. Colored arrows indicate the preferred solutions used for the tomographic inversion for each profile. Horizontal dashed black line corresponds to $\chi^2 = 1.1$, the adopted threshold value for the misfit function.

inverted following the same tomographic procedure used for the real data, using the same parameters as in our preferred solutions. If the resolution were perfect, the recovered model would reproduce the velocity anomaly pattern of the starting model. Regions that do resemble the anomaly pattern indicate that data are resolving lateral velocity variations of a length scale equal to the anomaly width.

[77] We show the results of two sets of corrugation tests in Figure C1. The first test was conducted for profile K1 using four different anomaly widths (i.e., half wavelength of the sinusoidal perturbation): 1.5, 2.0, 2.5 and 5.0 km (Figures C1a–C1d). The 1.5-km-wide anomaly pattern is recovered reasonably well up to a depth of 0.5 km below the seafloor. However, the amplitude of the recovered anomalies is smaller, particularly in areas of rough and/or deep seafloor. This is not surprising given the lower ray density at these locations (Figure 9, bottom). The maximum depth at which anomalies are well recovered increases with the size of the anomalies. For anomaly widths 1.5–2.5 km, the data resolve the anomalies down to the depth of approximately 0.5 km below the seafloor, while for an anomaly width of 5.0 km the data resolve the anomalies down to a depth of approximately 1.0 km below the seafloor. Thus, features as small as 1.5 km wide in the final velocity model (Figure 7) are meaningful and well resolved at subseafloor depths less than ~0.5 km within the shallow parts of the profile away from the profile ends, while features at scales of 5 km or larger

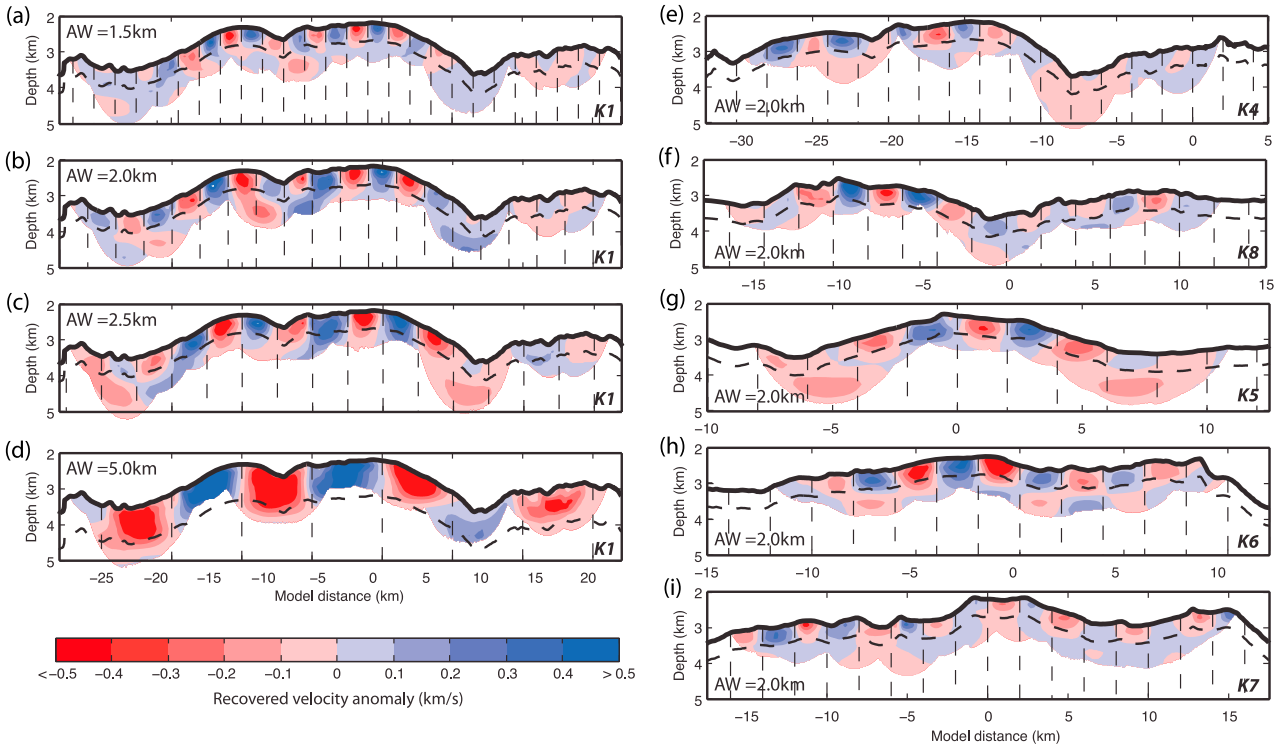

Figure C1. Results of lateral resolution tests. True anomaly pattern is created by a sine function with maximum amplitude of ±0.5 km s^{-1}, and vertical dashed lines show the positions of true anomaly equal to zero. Thick dashed lines denote estimates of maximum depth of good resolution. (a–d) Results of corrugation tests for profile K1, with varying anomaly widths (AW) indicated. Bold dashed lines are at a depth of 0.5 km in Figures C1a–C1c and at 1 km in Figure C1d. (e–i) Results of corrugation tests for the other five profiles with AW = 2.0 km. Bold dashed lines are at a depth of 0.5 km.

along the profile are meaningful at subseafloor depths to about 1.0 km.

[78] A second set of corrugation tests was conducted for the other five profiles using a constant anomaly width of 2.0 km (Figures C1e–C1i). In those tests, the depth to which the anomalies are well resolved is approximately 0.5 km. The main conclusion from these tests is that anomalies that are ~2.0 km wide and less than 0.5 km subseafloor can be trusted and interpreted, except at the ends of profiles where resolution is poorer.

C2. Velocity Uncertainty Estimate

[79] To estimate the uncertainty in our velocity models we followed a Monte Carlo approach [e.g., *Korenaga et al.*, 2000]. We constructed 100 different initial velocity models and used the observed traveltime with noise added to obtain 100 Monte Carlo solutions. Random Gaussian noise was added to the observed traveltime gradients, $N(0, \sigma = 30$ ms $km^{-1})$, following the method of *Zhang and Toksöz* [1998]. The 100 different initial velocity models were selected using the following procedure. First, we ran several 2-D inversions using a wide variety of initial models to constrain the range of 1-D models that converged to a stable and reliable solution. This was done to avoid using extreme initial 1-D models (e.g., with very high or low seafloor velocity, or unrealistic vertical velocity gradients) that cannot converge to an acceptable data fit. For the case of profile K7, Figure C2a shows the range of models explored (seafloor velocity 3 to 6 km s^{-1}, every 1 km s^{-1}, and vertical velocity gradient 0.25 to 3.25 s^{-1}, every 0.75 s^{-1}) and their resulting data fit expressed in terms of χ^2. We then selected 100 1-D models within the range of models that converge to a $\chi^2 \leq 2.5$ (Figure C2). Finally we ran 100 tomographic inversions using all the initial velocity models, following the same tomographic procedure used for the real data and using the same model parameterizations as in our preferred solutions. Assuming that all the Monte Carlo realizations have the same probability, the estimated velocity uncertainty can be approximated by the standard deviation of the

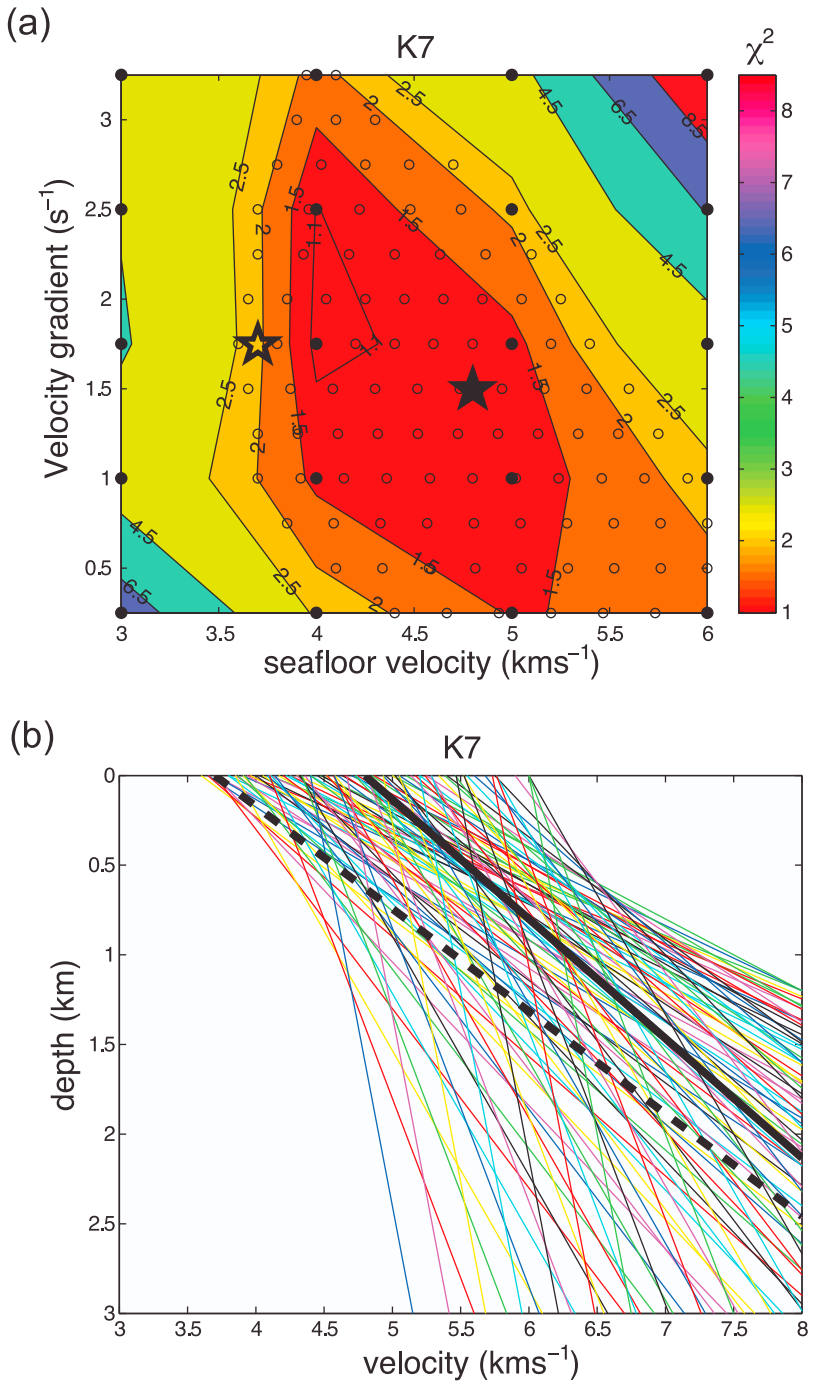

Figure C2. (a) Contour of traveltime residuals χ^2 (after five iterations) calculated for profile K7 using different seafloor velocities and vertical velocity gradients (black dots). The 100 black circles show equally spaced initial velocity structures used for estimating velocity uncertainties. The solid black star represents the best 1-D initial velocity model for profile K7, and the open black star shows the best average 1-D model for all lines. (b) The 100 1-D starting models for estimating the traveltime uncertainties for profile K7. The thick black line shows the starting model for profile K7 (Figure B1b), corresponding to the solid black star in Figure C2a, and the thick dashed line shows the average starting model (Figure B1b), corresponding to the open black star in Figure C2a.

100 Monte Carlo realizations [e.g., *Korenaga et al.*, 2000].

Acknowledgments

[80] We thank the captain, crew, and scientific party of R/V *Maurice Ewing* Cruise 0102 for their valuable assistance during the MCS field program and John Collins, who served as cruise Co–Chief Scientist with B.E.T. We also thank H. Dick and the WHOI geodynamics group for insightful discussions. H. Dick and M. Tivey generously shared geologic sample data on Kane OCC with us during the course of this study. This study benefited from insightful reviews by D. Shillington, D. Blackman, and an anonymous reviewer. This research was supported by NSF grants OCE-9987004 and OCE-0621660.

References

Auzende, J.-M., M. Cannat, P. Gente, J.-P. Henriet, T. Juteau, J. A. Karson, Y. Lagabrielle, C. Mével, and M. A. Tivey (1994), Observation of sections of oceanic crust and mantle cropping out on the southern wall of Kane FZ (N. Atlantic), *Terra Nova*, *6*, 143–148, doi:10.1111/j.1365-3121.1994.tb00647.x.

Baines, A. G., M. J. Cheadle, B. E. John, and J. J. Schwartz (2008), The rate of oceanic detachment faulting at Atlantis Bank, SW Indian Ridge, *Earth Planet. Sci. Lett.*, *273*(1–2), 105–114, doi:10.1016/j.epsl.2008.06.013.

Ballu, V., J. Dubois, C. Deplus, M. Diament, and S. Bonvalot (1998), Crustal structure of the Mid-Atlantic Ridge south of the Kane fracture zone from seafloor and sea surface gravity data, *J. Geophys. Res.*, *103*, 2615–2631, doi:10.1029/97JB02542.

Berge, P. A., G. J. Fryer, and R. H. Wilkens (1992), Velocity-porosity relationships in the upper oceanic crust: theoretical considerations, *J. Geophys. Res.*, *97*(B11), 15,239–15,254, doi:10.1029/92JB01464.

Blackman, D. K., B. Ildefonse, B. E. John, Y. Ohara, D. J. Miller, C. J. MacLeod, and Expedition 304/305 Scientists (2006), *Oceanic Core Complex Formation*, *Atlantis Massif, Proc. Integrated Ocean Drill. Program*, vol. 304/305, doi:10.2204/iodp.proc.304305.2006, Ocean Drill. Program, College Station, Tex.

Brown, J. R., and J. A. Karson (1988), Variations in axial processes on the Mid-Atlantic Ridge: The median valley of the MARK area, *Mar. Geophys. Res.*, *10*, 109–138, doi:10.1007/BF02424663.

Buck, W. R., L. L. Lavier, and A. N. B. Poliakov (2005), Modes of faulting at mid-ocean ridges, *Nature*, *434*, 719–723, doi:10.1038/nature03358.

Calvert, A. J. (1995), Seismic evidence for a magma chamber beneath the slow-spreading Mid-Atlantic Ridge, *Nature*, *377*, 410–414, doi:10.1038/377410a0.

Calvert, A. J., M. A. Fisher, S. Y. Johnson, and the SHIPS Working Group (2003), Along-strike variations in the shallow seismic velocity structure of the Seattle fault zone: Evidence for fault segmentation beneath Puget Sound, *J. Geophys. Res.*, *108*(B1), 2005, doi:10.1029/2001JB001703.

Canales, J. P., J. A. Collins, J. Escartín, and R. S. Detrick (2000a), Seismic structure across the rift valley of the Mid-Atlantic Ridge at 23°20′N (MARK area): Implications for crustal accretion processes at slow spreading ridges, *J. Geophys. Res.*, *105*, 28,411–28,425.

Canales, J. P., R. S. Detrick, J. Lin, J. A. Collins, and D. R. Toomey (2000b), Crustal and upper mantle seismic structure beneath the rift mountains and across a non-transform offset at the Mid-Atlantic Ridge (35°N), *J. Geophys. Res.*, *105*, 2699–2719, doi:10.1029/1999JB900379.

Canales, J. P., B. E. Tucholke, M. Xu, J. A. Collins, and D. L. Dubois (2008), Seismic evidence for large-scale compositional heterogeneity of oceanic core complexes, *Geochem. Geophys. Geosyst.*, *9*, Q08002, doi:10.1029/2008GC002009.

Cann, J. R., D. K. Blackman, D. K. Smith, E. McAllister, B. Janssen, S. Mello, E. Avgerinos, A. R. Pascoe, and J. Escartín (1997), Corrugated slip surfaces formed at ridge-transform intersections on the Mid-Atlantic Ridge, *Nature*, *385*, 329–332, doi:10.1038/385329a0.

Cannat, M., et al. (1995a), Thin crust, ultramafic exposures, and rugged faulting patterns at the Mid-Atlantic Ridge (22°–24°N), *Geology*, *23*, 49–52, doi:10.1130/0091-7613(1995)023<0049:TCUEAR>2.3.CO;2.

Cannat, M., et al. (1995b), *Proceedings of the Ocean Drilling Program, Initial Reports*, vol. 153, Ocean Drill Program, College Station, Tex.

Cannat, M., V. Mendel, E. Ruellan, K. Okino, J. Escartín, V. Combier, and M. Baala (2006), Modes of seafloor generation at a melt-poor ultraslow-spreading ridge, *Geology*, *34*(7), 605–608, doi:10.1130/G22486.1.

Carlson, R. L., and C. N. Herrick (1990), Densities and porosities in the oceanic crust and their variations with depth and age, *J. Geophys. Res.*, *95*(B6), 9153–9170, doi:10.1029/JB095iB06p09153.

Christensen, N. I. (2004), Serpentinites, peridotites, and seismology, *Int. Geol. Rev.*, *46*(9), 795–816, doi:10.2747/0020-6814.2746.2749.2795.

Cormier, M.-H., R. S. Detrick, and G. M. Purdy (1984), Anomalously thin crust in oceanic fracture zones: New seismic constraints from the Kane fracture zone, *J. Geophys. Res.*, *89*, 10,249–10,266.

deMartin, B. J., R. Reves-Sohn, J. P. Canales, and S. E. Humphris (2007), Kinematics and geometry of active detachment faulting beneath the Trans-Atlantic Geotraverse (TAG) hydrothermal field on the Mid-Atlantic Ridge, *Geology*, *35*(8), 711–714, doi:10.1130/G23718A.1.

Detrick, R. S., and G. M. Purdy (1980), The crustal structure of the Kane fracture zone from seismic refraction studies, *J. Geophys. Res.*, *85*, 3759–3778, doi:10.1029/JB085iB07p03759.

Detrick, R. S., et al. (1988), *Proceedings of the Ocean Drilling Program, Initial Reports*, vol. 106/109/111, Ocean Drill. Program, College Station, Tex.

Detrick, R. S., J. C. Mutter, P. Buhl, and I. I. Kim (1990), No evidence from multichannel reflection data for a crustal magma chamber in the MARK area on the Mid-Atlantic Ridge, *Nature*, *347*, 61–64, doi:10.1038/347061a0.

Detrick, R. S., R. S. White, and G. M. Purdy (1993), Crustal structure of North Atlantic fracture zones, *Rev. Geophys.*, *31*, 439–458, doi:10.1029/93RG01952.

Detrick, R. S., H. D. Needham, and V. Renard (1995), Gravity anomalies and crustal thickness variations along the Mid-Atlantic Ridge between 33°N and 40°N, *J. Geophys. Res.*, *100*, 3767–3787, doi:10.1029/94JB02649.

Dick, H. J. B., et al. (2000), A long in situ section of the lower ocean crust: Results of ODP Leg 176 drilling at the Southwest Indian ridge, *Earth Planet. Sci. Lett.*, *179*, 31–51, doi:10.1016/S0012-821X(00)00102-3.

Dick, H. J. B., M. A. Tivey, and B. E. Tucholke (2008), Plutonic foundation of a slow-spread ridge segment: The oceanic core complex at Kane Megamullion, 23°30′N, 45°20′W, *Geochem. Geophys. Geosyst.*, *9*, Q05014, doi:10.1029/2007GC001645.

Dunn, R. A., and D. R. Toomey (2001), Crack-induced seismic anisotropy in the oceanic crust across the East Pacific Rise (9° 30′N), *Earth Planet. Sci. Lett.*, *189*, 9–17, doi:10.1016/S0012-821X(01)00353-3.

Escartín, J., D. K. Smith, J. Cann, H. Schouten, C. H. Langmuir, and S. Escrig (2008), Central role of detachment faults in accretion of slow-spreading oceanic lithosphere, *Nature*, *455*, 790–794, doi:10.1038/nature07333.

Gente, P., R. A. Pockalny, C. Durand, C. Deplus, M. Maia, G. Ceuleneer, C. Mével, M. Cannat, and C. Laverne (1995), Characteristics and evolution of the segmentation of the Mid-Atlantic Ridge between 20°N and 24°N during the last 10 million years, *Earth Planet. Sci. Lett.*, *129*, 55–71, doi:10.1016/0012-821X(94)00233-O.

Grevemeyer, I., and W. Weigel (1997), Increase of seismic velocities in upper oceanic crust: The ''superfast'' spreading East Pacific Rise at 14°14′S, *Geophys. Res. Lett.*, *24*(3), 217–220, doi:10.1029/96GL04005.

Grimes, C. B., B. E. John, M. J. Cheadle, and J. L. Wooden (2008), Protracted construction of gabbroic crust at a slow-spreading ridge: Constraints from 206Pb/238U zircon ages from Atlantis Massif and IODP Hole U1309D (30°N MAR), *Geochem. Geophys. Geosyst.*, *9*, Q08012, doi:10.1029/2008GC002063.

Harding, A. J., J. A. Orcutt, M. E. Kappus, E. E. Vera, J. C. Mutter, P. Buhl, R. S. Detrick, and T. M. Brocher (1989), The structure of young oceanic crust at 13°N on the East Pacific Rise from expanding spread profiles, *J. Geophys. Res.*, *94*, 12,163–12,196.

Houtz, R. E., and J. Ewing (1976), Upper crustal structure as a function of plate age, *J. Geophys. Res.*, *81*, 2490–2498, doi:10.1029/JB081i014p02490.

Ildefonse, B., D. K. Blackman, B. E. John, Y. Ohara, D. J. Miller, C. J. MacLeod, and Integrated Ocean Drilling Program Expeditions 304/305 Science Party (2007), Oceanic core complexes and crustal accretion at slow-spreading ridges, *Geology*, *35*(7), 623–626, doi:10.1130/G23531A.1.

Johnson, H. P., and S. W. Semyan (1994), Age variation in the physical properties of oceanic basalts: Implications for crustal formation and evolution, *J. Geophys. Res.*, *99*(B2), 3123–3134, doi:10.1029/93JB00717.

Karson, J. A., and H. J. B. Dick (1983), Tectonics of ridge-transform intersection at the Kane Fracture Zone, *Mar. Geophys. Res.*, *6*, 51–98, doi:10.1007/BF00300398.

Karson, J. A., et al. (1987), Along-axis variations in seafloor spreading in the MARK area, *Nature*, *328*, 681–685, doi:10.1038/328681a0.

Kelemen, P. B., E. Kikawa, and D. J. Miller (2004), *Proceedings of the Ocean Drilling Program, Initial Reports*, vol. 209, Ocean Drill. Program, College Station, Tex.

Kong, L. S. L., R. S. Detrick, P. J. Fox, L. A. Mayer, and W. B. F. Ryan (1988), The morphology and tectonics of the MARK area from SeaBeam and Sea MARC I observations (Mid-Atlantic Ridge 23°N), *Mar. Geophys. Res.*, *10*, 59–90, doi:10.1007/BF02424661.

Kong, L. S. L., S. C. Solomon, and G. M. Purdy (1992), Microearthquake characteristics of a mid-ocean ridge along-axis high, *J. Geophys. Res.*, *97*, 1659–1685, doi:10.1029/91JB02566.

Korenaga, J., W. S. Holbrook, G. M. Kent, P. B. Kelemen, R. S. Detrick, H.-C. Larsen, J. R. Hopper, and T. Dahl-Jensen (2000), Crustal structure of the southeast Greenland margin from joint refraction and reflection seismic tomography, *J. Geophys. Res.*, *105*, 21,591–21,614.

Kuster, G. T., and M. N. Töksoz (1974), Velocity and attenuation of seismic waves in two-phase media: Part I. Theoretical formulations, *Geophysics*, *39*(5), 587–606, doi:10.1190/1.1440450.

Lin, J., G. M. Purdy, H. Schouten, J.-C. Sempéré, and C. Zervas (1990), Evidence from gravity data for focused magmatic accretion along the Mid-Atlantic Ridge, *Nature*, *344*, 627–632, doi:10.1038/344627a0.

Lizarralde, D., J. B. Gaherty, J. A. Collins, G. Hirth, and S. D. Kim (2004), Spreading-rate dependence of melt extraction at mid-ocean ridges from mantle seismic refraction data, *Nature*, *432*, 744–747, doi:10.1038/nature03140.

MacLeod, C. J., et al. (2002), Direct geological evidence for oceanic detachment faulting: The Mid-Atlantic Ridge, 15°45′N, *Geology*, *30*(10), 879–882, doi:10.1130/0091-7613(2002)030<0879:DGEFOD>2.0.CO;2.

Maia, M., and P. Gente (1998), Three-dimensional gravity and bathymetry analysis of the Mid-Atlantic Ridge between 20°N and 24°N: Flow geometry and temporal evolution of the segmentation, *J. Geophys. Res.*, *103*, 951–974, doi:10.1029/97JB01635.

Mével, C., M. Cannat, P. Gente, E. Marion, J.-M. Auzende, and J. A. Karson (1991), Emplacement of deep crustal and mantle rocks on the west median valley wall of the MARK area (MAR, 23°N), *Tectonophysics*, *190*, 31–53, doi:10.1016/0040-1951(91)90353-T.

Miller, D. J., and N. I. Christensen (1997), Seismic velocities of lower crustal and upper mantle rocks from the slow spreading Mid-Atlantic Ridge, south of the Kane transform zone (MARK), *Proc. Ocean Drill. Program Sci. Results*, *153*, 437–454.

Minshull, T. A., R. S. White, J. C. Mutter, P. Buhl, R. S. Detrick, C. A. Williams, and E. Morris (1991), Crustal structure at the Blake Spur fracture zone from expanding spread profiles, *J. Geophys. Res.*, *96*, 9955–9984, doi:10.1029/91JB00431.

Morris, E., and R. S. Detrick (1991), Three-dimensional analysis of gravity anomalies in the MARK area, Mid-Atlantic Ridge 23°N, *J. Geophys. Res.*, *96*, 4355–4366, doi:10.1029/90JB02173.

Ohara, Y., T. Yoshida, and S. Kasuga (2001), Giant megamullion in the Parece Vela Backarc basin, *Mar. Geophys. Res.*, *22*, 47–61, doi:10.1023/A:1004818225642.

Okino, K., K. Matsuda, D. M. Christie, Y. Nogie, and K. Koizumi (2004), Development of oceanic detachment and asymmetric spreading at the Australian-Antarctic Discordance, *Geochem. Geophys. Geosyst.*, *5*, Q12012, doi:10.1029/2004GC000793.

Pockalny, R. A., R. S. Detrick, and P. J. Fox (1988), Morphology and tectonics of the Kane transform from SeaBeam bathymetry data, *J. Geophys. Res.*, *93*, 3179–3193, doi:10.1029/JB093iB04p03179.

Pockalny, R. A., A. Smith, P. Gente (1995), Spatial and temporal variability of crustal magnetization of a slow spreading ridge: Mid-Atlantic Ridge (20°–24°N), *Mar. Geophys. Res.*, *17*, 301–320, doi:10.1007/BF01203467.

Purdy, G. M., and R. S. Detrick (1986), Crustal structure of the Mid-Atlantic ridge at 23°N from seismic refraction studies, *J. Geophys. Res.*, *91*, 3739–3762, doi:10.1029/JB091iB03p03739.

Reston, T. J., W. Weinrebe, I. Grevemeyer, E. R. Flueh, N. C. Mitchell, L. Kirstein, C. Kopp, H. Kopp, and participants of *Meteor* 47/2 (2002), A rifted inside corner massif on the

Mid-Atlantic Ridge at 5°S, *Earth Planet. Sci. Lett.*, *200*, 255–269, doi:10.1016/S0012-821X(02)00636-2.

Schulz, R. J., R. S. Detrick, and S. P. Miller (1988), Two-and three-dimensional inversions of magnetic anomalies in the MARK area (Mid-Atlantic Ridge 23°N), *Mar. Geophys. Res.*, *10*, 41–57, doi:10.1007/BF02424660.

Schwartz, J. J., B. E. John, M. J. Cheadle, E. A. Miranda, C. B. Grimes, J. L. Wooden, and H. J. B. Dick (2005), Dating the growth of oceanic crust at a slow-spreading ridge, *Science*, *310*, 654–657, doi:10.1126/science.1116349.

Searle, R. C., M. Cannat, K. Fujioka, C. Mével, H. Fujimoto, A. Bralee, and L. M. Parson (2003), FUJI Dome: A large detachment fault near 64°E on the very slow-spreading southwest Indian Ridge, *Geochem. Geophys. Geosyst.*, *4*(8), 9105, doi:10.1029/2003GC000519.

Smith, D. K., J. R. Cann, and J. Escartín (2006), Widespread active detachment faulting and core complex formation near 13°N on the Mid-Atlantic Ridge, *Nature*, *442*, 440–443, doi:10.1038/nature04950.

Smith, D. K., J. Escartín, H. Schouten, and J. R. Cann (2008), Fault rotation and core complex formation: Significant processes in seafloor formation at slow-spreading mid-ocean ridges (Mid-Atlantic Ridge, 13°–15°N), *Geochem. Geophys. Geosyst.*, *9*, Q03003, doi:10.1029/2007GC001699.

Stephen, R. A. (1981), Seismic anisotropy observed in upper oceanic crust, *Geophys. Res. Lett.*, *8*(8), 865–868, doi:10.1029/GL008i008p00865.

Stephen, R. A. (1985), Seismic anisotropy in the upper oceanic crust, *J. Geophys. Res.*, *90*(B13), 11,383–11,396.

Toomey, D. R., G. M. Purdy, and S. C. Solomon (1988), Microearthquakes beneath the median valley of the Mid-Atlantic Ridge near 23°N: Tomography and tectonics, *J. Geophys. Res.*, *93*, 9093–9112, doi:10.1029/JB093iB08p09093.

Tucholke, B. E., J. Lin, and M. C. Kleinrock (1996), Mullions, megamullions, and metamorphic core complexes on the Mid-Atlantic Ridge, *Eos Trans. AGU*, *77*, Fall Meet. Suppl., F724.

Tucholke, B. E., J. Lin, and M. C. Kleinrock (1998), Megamullions and mullion structure defining oceanic metamorphic core complexes on the Mid-Atlantic Ridge, *J. Geophys. Res.*, *103*, 9857–9866, doi:10.1029/98JB00167.

Tucholke, B. E., K. Fujioka, T. Ishihara, G. Hirth, and M. Kinoshita (2001), Submersible study of an oceanic megamullion in the central North Atlantic, *J. Geophys. Res.*, *106*(B8), 16,145–16,161.

Tucholke, B. E., M. D. Behn, R. Buck, and J. Lin (2008), The role of melt supply in detachment faulting and the formation of oceanic core complexes, *Geology*, *36*(6), 455–458, doi:10.1130/G24639A.

Vera, E. E., J. C. Mutter, P. Buhl, J. A. Orcutt, A. J. Harding, M. E. Kappus, R. S. Detrick, and T. M. Brocher (1990), The structure of 0- to 0.2-m.y.-old oceanic crust at 9°N on the East Pacific Rise from expanded spread profiles, *J. Geophys. Res.*, *95*, 15,529–15,556.

Whitehead, J. A., H. J. B. Dick, and H. Schouten (1984), A mechanism for magmatic accretion under spreading centers, *Nature*, *312*, 146–148, doi:10.1038/312146a0.

Wilkens, R. H., G. J. Fryer, and J. Karsten (1991), Evolution of porosity and seismic structure of upper oceanic crust: Importance of aspect ratios, *J. Geophys. Res.*, *96*, 17,981–17,995.

Williams, C. M., M. A. Tivey, and M. D. Behn (2006), The magnetic structure of Kane megamullion: Results from marine magnetic anomalies, paleomagnetic data and thermal modeling, *Eos Trans. AGU*, *87*(52), Fall Meet. Suppl., Abstract T42A-03.

Zelt, B. C., B. Taylor, J. R. Weiss, A. M. Goodliffe, M. Sachpazi, and A. Hirn (2004), Streamer tomography velocity models for the Gulf of Corinth and Gulf of Itea, Greece, *Geophys. J. Int.*, *159*, 333–346, doi:10.1111/j.1365-246X.2004.02388.x.

Zelt, C. A., and P. J. Barton (1998), Three-dimensional seismic refraction tomography: A comparison of two methods applied to data from the Faeroe Basin, *J. Geophys. Res.*, *103*(B4), 7187–7210, doi:10.1029/97JB03536.

Zelt, C. A., and D. A. Forsyth (1994), Modeling wide-angle seismic data for crustal structure: Southeastern Grenville Province, *J. Geophys. Res.*, *99*(B6), 11,687–11,704.

Zhang, J., and M. N. Toksöz (1998), Nonlinear refraction traveltime tomography, *Geophysics*, *63*, 1726–1737, doi:10.1190/1.1444468.